

**ULE CAVITY APPLICATIONS AND OTHER DEVELOPMENTS
AT THE TRIUMF FRANCIUM BEAM TRAPPING FACILITY**

by

A.C. DeHart

A Thesis submitted to the Faculty of Graduate Studies of

The University of Manitoba

in partial fulfillment of the requirements of the degree of

Master of Science

Department of Physics and Astronomy

University of Manitoba

Winnipeg, Manitoba, Canada

Copyright © 2018 by A.C. DeHart

ABSTRACT

The Francium Group at TRIUMF is preparing to study the parity-violating electric dipole amplitude for the $7s \rightarrow 8s$ transition in francium. The parity-violating weak force contributes very small perturbations of electron wave functions which can be explored with spectroscopy for this transition in heavy alkali atoms. This thesis reports on isotope-shift measurements for $7s_{1/2} \rightarrow 8s_{1/2}$ and transitions in isotopes $^{208-211}\text{Fr}$ and ^{213}Fr which will help us interpret future atomic parity non-conservation investigations for this element. An ultra low expansion cavity has been implemented in a new laser locking system to support such measurements. With this cavity, we have begun preliminary single-photon Stark-shift investigations of the analogous $5s \rightarrow 6s$ transition in ^{87}Rb . This thesis also reports on other developments at the francium trapping facility such as new transparent indium tin oxide electric field plates for Stark-shift investigations and implementing new OTS dryfilm coatings in our capture cell.

Acknowledgments

I owe my sincerest thanks to Gerald Gwinner and Mukut Kalita for their guidance throughout my graduate career and significant contributions to this thesis.

Contents

Abstract	i
Acknowledgments	ii
Contents	iii
List of Figures	v
Abbreviations	vii
1 INTRODUCTION	1
2 DEVELOPMENTS	8
2.1 ULE Laser Locking Cavity	8
2.1.1 Cavity Selection and ULE Properties	9
2.1.2 ULE Temperature Control Performance	11
2.1.3 PDH Locking Technique	15
2.2 ITO Electric Field Plates	20
3 Spectroscopy	22
3.1 Fr $7s \rightarrow 8s$ Two-Photon	22
3.2 Rb $5s \rightarrow 6s$ One-Photon Stark-Induced	26

3.2.1	Theory for DC Scalar Polarizability Measurement	26
3.2.2	Parameters and Results of Experiment	28
3.2.3	Projecting Minimum Error in Scalar Polarizability	32
4	OUTLOOK	35
A	IGBT Current Switch	37
B	Flapper and Foil Upgrades	45
C	Neutralizer Safety Upgrades	49
D	OTS Cell Coating	52
E	Software	55
	Bibliography	59

List of Figures

1.1	Measurements of the weak neutral current strength as a function of momentum transfer	2
1.2	Illustration of our francium capture technique	3
1.3	Energy level diagram for our trapping, repumping, and probing techniques in ^{87}Rb and ^{211}Fr	5
2.1	ULE cavity in hand.	9
2.2	Temperature control system for ULE cavity.	10
2.3	Circuit diagram for analog temperature control circuit.	11
2.4	Raspberry Pi computer for monitoring and logging ULE and room temperature data.	12
2.5	Long and short term temperature measurements of the ULE.	13
2.6	ULE cavity vacuum system without insulating shell.	14
2.7	Signal paths through the components in our ULE locking scheme.	15
2.8	Illustrations of how an error signal is produced for ULE locking schemes. . .	16
2.9	Exposed Toptica DL100 laser block.	18
2.10	ITO plates before installation.	21

3.1	Typical two-photon spectroscopy data for our scan over the $7s(F=5) \rightarrow 8s(F=5)$ transition in ^{211}Fr	25
3.2	Isotope shifts of the D1 line against the $7s \rightarrow 8s$ transition for isotopes $^{208-211}\text{Fr}$ and ^{213}Fr	26
3.3	^{87}Rb Stark-shift data set fit to a Voigt function.	29
3.4	Rubidium one-photon Stark-shift figures	31
4.1	IGBT circuit in ‘on’ and ‘off’ configurations	38
4.2	Images and circuits of the original IGBT board	39
4.3	Prototype of the IGBT switch.	40
4.4	Configuration for three trials to test the performance of our IGBT circuit.	42
4.5	Examining a 20 ms IGBT duty cycle while supplied 50 A	44
4.6	Model and figures of our neutralizer and flapper apparatus.	46
4.7	Images of damaged yttrium and zirconium foils.	48
4.8	Neutralizer heater control and safety systems before and after August 2016.	50
4.9	Current-time curves of TA35 breaker used to protect neutralizer foil.	51
4.10	Image of preparation stages for OTS coating	53

Abbreviations

AOM	acousto-optic modulator
CF	ConFlat
CSV	comma-separated variable
DAMOP	Division of Atomic, Molecular, and Optics Physics
EOM	electro-optic modulator
FTF	Francium Trapping Facility
GUI	graphical user interface
IGBT	insulated-gate bipolar transistor
ITO	indium tin oxide
MOT	magneto-optical trap
OTS	octadecyltrichlorosilane
PDH	Pound-Drever-Hall
PID	proportional-integral-derivative
PMT	photomultiplier tube
R-EOM	resonant electro-optic modulator

R-Pi	Raspberry Pi
SC-77	dichloromethylsilane
SRS	Stanford Research Systems
TEM _{0,0}	lowest order transverse electromagnetic mode
TTL	transistor-transistor logic
ULE	ultra low expansion

Chapter 1

INTRODUCTION

Studying atomic parity non-conservation (APNC) with francium can give us a window to into ‘new’ physics and corrections to the Standard Model [1]. Z-bosons interacting between electrons and quarks within the nucleus give rise to parity-violating effects where they provide a means for otherwise forbidden electric dipole transitions to occur between states of the same parity [2]. Many different experiments have studied weak neutral currents, as shown in Figure 1.1, but APNC studies are one of the three experiments exploring weak neutral current strength at very low momentum transfer [3].

In general, APNC studies are done using atoms with large proton number, Z , where electron wave functions can overlap more with larger nuclei and APNC effects scale as a function of Z^3 [2]. The atomic structure should also be well understood while pursuing weak interaction physics, lending large alkali atoms to this sort of research; the single valence electron of alkali atoms greatly simplifies theoretical models of atomic structure. For these two reasons, francium is the best candidate to pursue APNC experiments being the heaviest alkali element. Since francium has no stable isotopes, it needs to be produced by nuclear

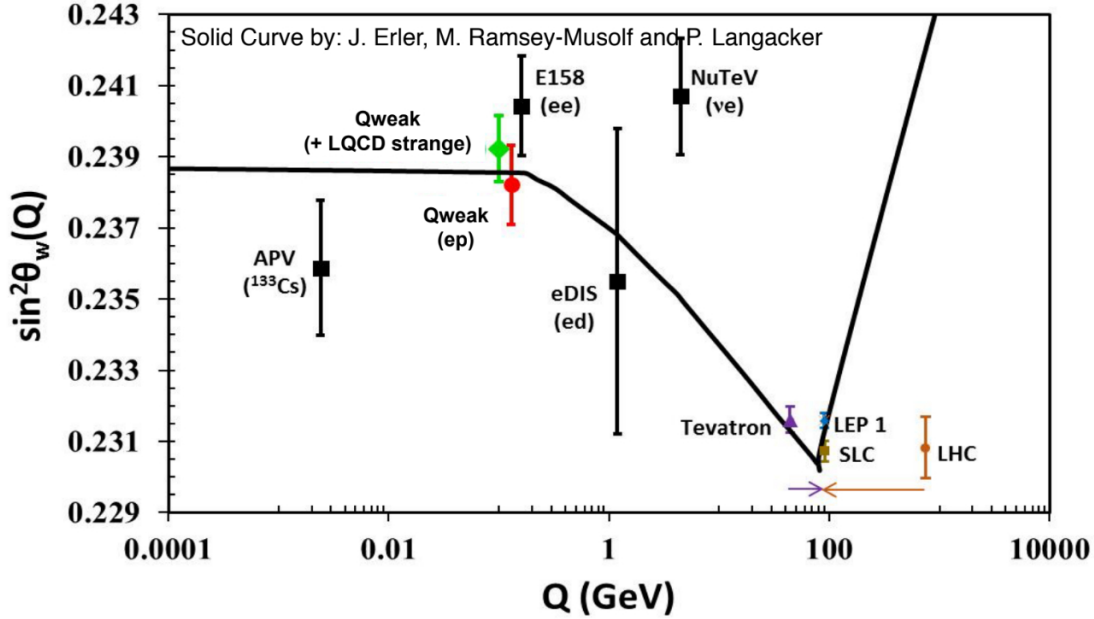


Figure 1.1: Measurements of the weak neutral current strength as a function of momentum transfer with θ_W as the Weinberg angle. Here APNC is labeled with APV for atomic parity-violation. Figure taken from the final Qweak announcement [4].

reactions on-line at an accelerator.

TRIUMF’s Isotope Separator and Accelerator (ISAC) facility produces and transports beams of ionized francium to the Francium Trapping Facility (FTF). Following Figure 1.2, this ionized beam enters our capture vacuum chamber, strikes and embeds itself onto a neutralizing zirconium foil. This foil is then pneumatically rotated up to the base of a Pyrex cell. Our conductive neutralizer is connected by feedthrough leads to an external power supply which allows us to heat the foil. Heating this foil releases neutral francium from its surface where francium now bounces its way up the stem of the Pyrex cell. The application of a ‘dryfilm’ coating helps prevent chemical bonds from forming between the alkali atoms and the surface of the cell, resulting in a greater number of atoms to freely bounce into the bulb of the cell where they can be captured by a magneto-optical trap (MOT) [5].

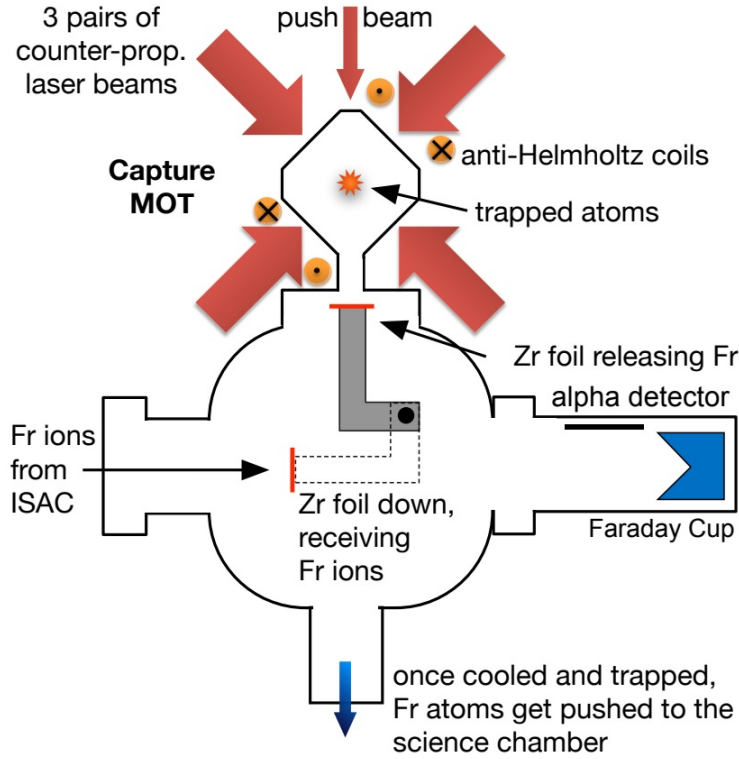


Figure 1.2: Illustration of our francium capture methods. Figure is taken from G. Gwinner’s 2017 NSERC proposal.

The MOT provides spacial and velocity dependent forces to trap atoms at a central point sustained by two primary components: (1) a set of three laser beams overlapping the center of the trap with mirrors to reflect the beams back on themselves as well as (2) a magnetic field gradient produced by a pair of anti-Helmholtz coils [6].

For the sake of demonstration, let us assume our atom is a two-level system in one dimension. Trapping light of the same frequency and opposite circular polarization is sent to the atom from both sides. The frequency of this light is red-detuned from the frequency of the two-level atomic transition by a few line widths. Because of the Doppler effect, a moving atom will observe blue-shifted light from the direction it is traveling. The atom will then absorb more photons from that direction and spontaneously re-emit photons in

an unpreferred direction, losing kinetic energy with each re-emitted photon. This velocity dependent ‘optical molasses’ technique is then expanded to three dimensions in our MOT.

The coils help facilitate a position dependent force for the MOT where they produce a magnetic field that is zero at the center of the trap and increases with distance away from the mid-plane between the coils. The Zeeman splitting effect increases as a function of distance from the center of the trap, lifting the degeneracies of the electron energy levels. In a one-dimensional example for a two-level atom, say that it is positioned to the right of the origin. The upper level $J = 1$ splits into levels $m = 1, 0,$ and -1 such that our red-detuned light is now resonant with the $J = 0, m = 0 \rightarrow J = 1, m = -1$ transition. If the atom was displaced to the left, the trap light would then be resonant with the $J = 0, m = 0 \rightarrow J = 1, m = 1$ transition. We can choose the circular polarization of the trap laser such that it is σ_- coming from the right and σ_+ coming from the left. This way, the atoms will prefer to absorb photons from the direction the atom is displaced, getting pushed back to the origin. This concept is again applied in three dimensions for our MOT.

The alkali atoms we trap do not have this simplified two-level structure, but the principles of the MOT work well when we impose a two-level configuration. We can describe a MOT in ^{87}Rb where the physics can be applied to analogous hyperfine levels in isotopes of other alkalis. Following the left side of Figure 1.3, the two-level transition we focus on for trapping is between the $5s_{1/2} F = 2$ and $5p_{3/2} F = 3$ states. Because of the selection rules and the linewidth of our trapping laser and the states themselves, an undesirable $5s_{1/2} F = 2 \rightarrow 5p_{3/2} F = 2$ transition can occur where this excited state could decay back to the $5s_{1/2} F = 1$ state. Atoms in this ‘dark’ state are no longer resonant with our trap light, so we repump them with a second laser to excite the valence electron back to the $5p_{3/2} F = 2$

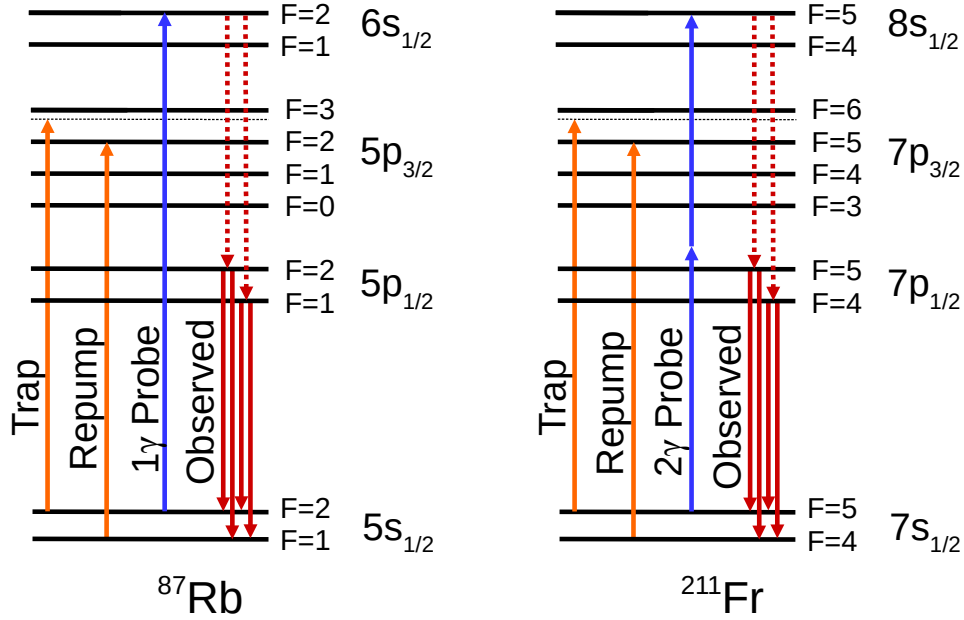


Figure 1.3: Energy level diagram for our MOT when studying (left) one-photon $5s \rightarrow 6s$ spectroscopy in ^{87}Rb and (right) two-photon $7s \rightarrow 8s$ spectroscopy in ^{211}Fr .

state. From here we want the valence electron to decay back to the $5s_{1/2}$ $F = 2$ state to make them accessible to our trap light again. If they fall back to the $5s_{1/2}$ $F = 1$ state, they will continue to be repumped until they return to the $5s_{1/2}$ $F = 2$ and repopulate the $5s_{1/2}$ $F = 2 \rightarrow 5p_{3/2}$ $F = 3$ cycle.

After we initially neutralize and trap francium in our upper chamber, we perform a cold transfer to a second ‘science’ chamber MOT which has the equipment and environment we require for our spectroscopy, including well controlled electric and magnetic fields. In this chamber, we will eventually pursue spectroscopy of the forbidden electric dipole $7s \rightarrow 8s$ transition, $E1_{\text{pnc}}$, so we can extract the weak charge of francium from it. This transition is impossible to observe on its own having an oscillator strength of $f \approx 10^{-20}$, but we can detect it through interference with a stronger magnetic dipole amplitude $M1$ ($f \approx 10^{-11}$)

and an allowed Stark-induced electric dipole amplitude, $E1_{\text{Stark}}$. $E1_{\text{Stark}}$ could easily drown out the $M1$ and $E1_{\text{pnc}}$ amplitudes, but we can control the strength of the amplitude with an external electric field and optimize it for interference with $E1_{\text{pnc}}$ [7]. The transition rate R for the $7s \rightarrow 8s$ transition in francium is

$$R \propto |E1_{\text{Stark}} + M1 + E1_{\text{pnc}}|^2, \quad (1.1)$$

where higher order amplitudes are small and neglected. $E1_{\text{Stark}}$ can be expressed in terms of scalar and vector polarizabilities, α and β , in the expression

$$E1_{\text{Stark}} = \alpha \vec{E} \cdot \vec{\epsilon} \delta_{F,F'} \delta_{m,m'} + i\beta (\vec{E} \times \vec{\epsilon}) \cdot \langle F'm' | \vec{\sigma} | Fm \rangle \quad (1.2)$$

where $\vec{\epsilon}$ is the oscillating electric field of the laser radiation exciting the transition, and $\vec{\sigma}$ are the Pauli spin matrices. In our experiment, we will excite a $\Delta F = \pm 1$ transition causing the α term to vanish, so the cross term $E1_{\text{pnc}}E1_{\text{Stark}}$ from Equation 1.1 now relies on the β term from Equation 1.2. Changing the direction of the external electric field causes a parity flip in our system. The parity-conserving $E1_{\text{Stark}}$ amplitude will change sign while the parity-violating $E1_{\text{pnc}}$ amplitude will not, causing an asymmetry in fluorescence between rates R_+ and R_- at opposite field directions. With these different rates, we can work our way back to get $E1_{\text{pnc}}$ relative to $E1_{\text{Stark}}$ from

$$\frac{R_+ - R_-}{R_+ + R_-} \propto \frac{\text{Im } E1_{\text{pnc}}}{\beta E}. \quad (1.3)$$

In this way, we determine $E1_{\text{pnc}}$ with respect to the transition amplitude β . The spectroscopy

laser that stimulates the $7s \rightarrow 8s$ transition will need to be stabilized to the 100 kHz level if we intend to make meaningful measurements. Before establishing β , it will be useful to characterize our science chamber and establish potential systematic issues in our spectroscopy methods by measuring α from Equation 1.2. Because we will likely pursue APNC studies in several isotopes of francium, it will also be helpful to experimentally determine how the frequency of the $7s \rightarrow 8s$ transition changes between a few of our favorite francium isotopes.

While making these preparations for francium spectroscopy, we practice applying all of our techniques first in ^{87}Rb while off-line. Though APNC effects in rubidium are significantly reduced, the ground state ns to np and $(n+1)s$ transitions in both elements are similar enough that we can perform the same trapping, repumping, and spectroscopy with the same lasers and equipment with minor tuning adjustments.

This thesis reports on the development of an ultra-stable optical reference cavity for our spectroscopy lasers as well as new francium spectroscopy and several hardware developments at the FTF.

Chapter 2

DEVELOPMENTS

2.1 ULE Laser Locking Cavity

To facilitate measurements of polarizability and transition rates of francium, our spectroscopy laser (or probe laser) will need to be frequency stabilized to the 100 kHz level. Francium itself cannot be used as a frequency reference because it has no stable isotopes. We could lock our probe laser to a stabilized HeNe laser using a computer controlled feedback system, but this technique would only be able to stabilize our probe laser to the 1 MHz level [8, 9]. We hope to satisfy our requirements with the development of a laser locking scheme that uses the Pound-Drever-Hall (PDH) method with the implementation of an ultra-stable Fabry-Perot cavity. In theory, locking our spectroscopy laser to this cavity can frequency stabilize the laser up to the level of the cavity's stability, on the order of 1.5 kHz.

2.1.1 Cavity Selection and ULE Properties

We purchased a custom 50 mm diameter, 100 mm long cavity from Advanced Thin Films to serve as our frequency reference, as shown in Figure 2.1. Advanced Thin Films manufacture cavities from ultra low expansion (ULE) Corning glass where the effects of thermal length expansion vanish at a specific temperature; the stability of our cavity is a parabolic function of temperature where the most stable temperature of the cavity is at the bottom of this parabola, called the zero crossing temperature. Temperature stability at the zero crossing temperature is the crucial aspect behind the performance of the ULE cavity. Previous work done by J. Alnis shows that maintaining a ULE cavity 0.5°C from this zero crossing temperature with a stability of 5 mK can result in a total frequency stability of 1.5 kHz [10]. This would correspond to a fractional uncertainty of frequency on the order of 10^{-12} for our scanning lasers. In an optimistic scenario where we have the same temperature stability but maintain the ULE cavity's temperature 0.1°C from the zero crossing temperature, we can expect a total frequency stability of 250 Hz. Both of these scenarios would be more than sufficient for our spectroscopy requirements.



Figure 2.1: This is an image of our ULE cavity in hand.

Our cavity was sent to Stable Laser Systems to determine its zero crossing temperature

which was measured to be 24.5 ± 1 °C. This is above the 18.5 ± 2 °C ambient temperature of our lab, so we only needed to develop a heating system to maintain the cavity’s temperature, as illustrated in Figure 2.2. To do this, the cavity was first placed in a 4.5” Kimball Physics vacuum chamber to help prevent frequency shifts due to spurious humidity and pressure changes. This assembly is then surrounded by an inch of foam thermal insulation pressed into an aluminum box. 0.5” holes are cut into the foam and aluminum box to make the cavity accessible with our optics. Isolating the 4 °C temperature swings of the lab is the greatest challenge in maintaining the cavity’s temperature. Two 10 k Ω thermistors (Honeywell 192-103LEV-A01, $\beta = 3974$) are taped directly onto the vacuum chamber [11]. The resistance of one is measured by a custom analog temperature control circuit, shown in Figure 2.3, that applies feedback to a heater power supply where the resistance of the other thermistor is measured by a Raspberry Pi computer that continuously records data.

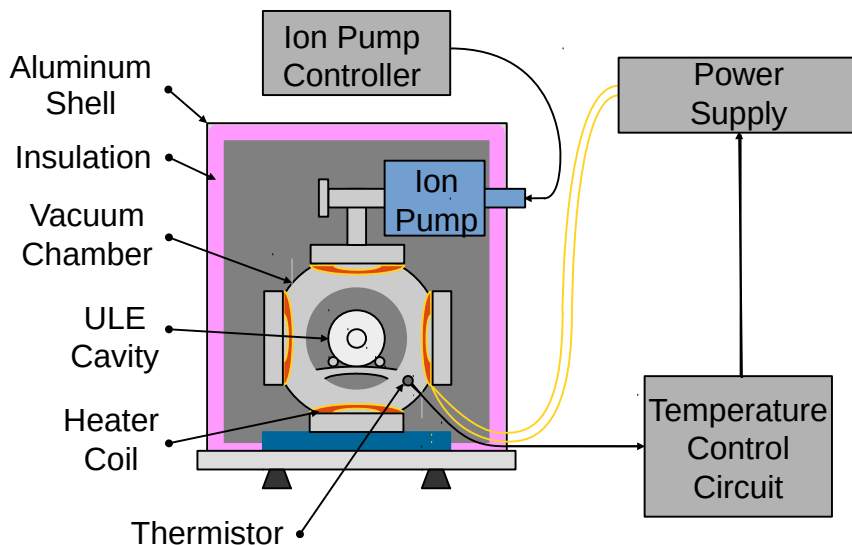


Figure 2.2: An illustration of the temperature control system for the ULE cavity.

The temperature control circuit was originally designed by M. Kalita with minor changes due to part availability [12]. Following Figure 2.3, the resistance of a thermistor and po-

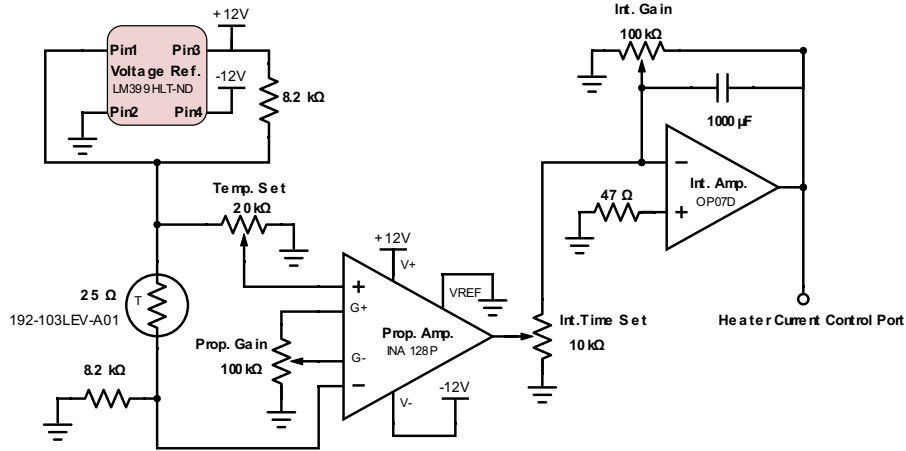


Figure 2.3: Circuit diagram for the analog temperature control system.

tentiometer is compared by the instrumentation amplifier (INA128) where both resistive devices are connected to a stable voltage reference (LM399HLT-ND) on their side opposite the INA128. If there is a difference in resistance of the two components, the INA128 will sense an imbalance in input potentials. When this happens, the INA128 outputs a non-zero voltage which is amplified, integrated, then sent to the heating power supply. Our heater power supply rejects negative voltage inputs corresponding to our system being too hot, but does respond to positive voltage inputs when the system is too cold by applying current through 19.32 m of 19 AWG wire amounting to 0.5Ω of resistance wrapped around our vacuum chamber, heating the system.

2.1.2 ULE Temperature Control Performance

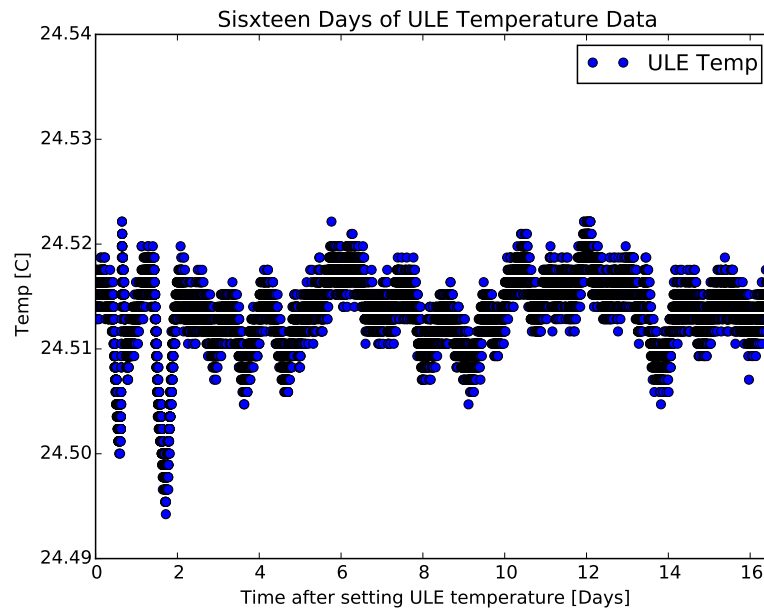
The second thermistor attached to our ULE vacuum chamber is connected to an external Raspberry Pi (R-Pi) computer, as shown in Figure 2.4. The thermal time constant of the insulated vacuum chamber is measured to be 7.6 hours where our R-Pi is programmed to

measure the resistance of devices installed to it once every minute. This computer then converts resistance measurements to temperature with appropriate Steinhart-Hart coefficients for the installed thermistors and appends the results to a text log [13]. Figure 2.5 reports the temperature measured with this method over sixteen days. The large room temperature fluctuations ($\pm 2^\circ\text{C}$) do not correspond to the seemingly random and small temperature changes of the ULE cavity. This means the combined insulation and temperature feedback circuit are performing well to prevent the room temperature swings from influencing the ULE temperature, where these small fluctuations of a few milliKelvin are well below the absolute accuracy of our thermistors as reported by the manufacturer to be $\pm 0.5^\circ\text{C}$.

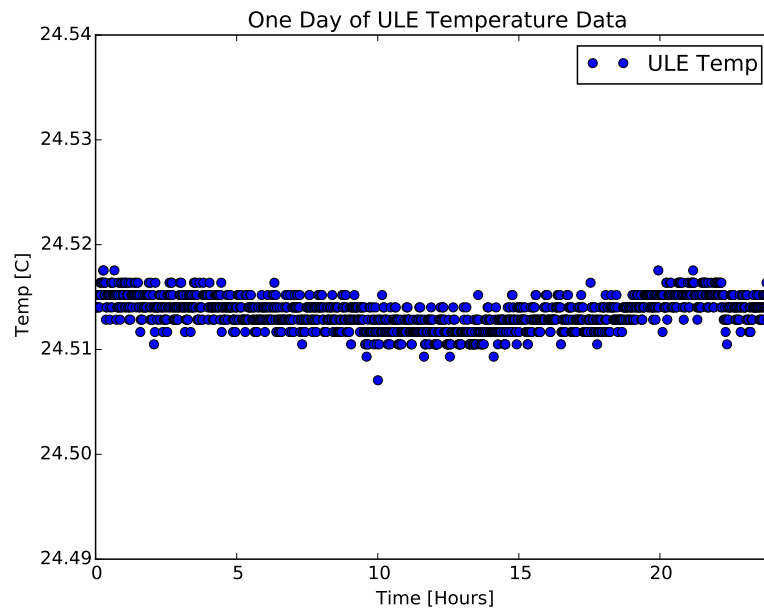


Figure 2.4: Raspberry Pi (R-Pi) computer for monitoring and logging ULE and room temperature data.

Because of the uncertainty in the absolute temperature of our cavity ($\pm 0.5^\circ\text{C}$) and the uncertainty in the zero crossing temperature of the ULE material ($\pm 1^\circ\text{C}$), the frequency stability of the cavity can be off by 5 kHz if the temperature of the ULE was offset by



(a)



(b)

Figure 2.5: (a) ULE temperature data for a sixteen day period. (b) The last 24 hours of the set that is shown in (a). Note that we are approaching the limits of the analog to digital conversion of our R-Pi computer, which presents as small discrete temperature steps in our figures.

one total standard deviation of $1.5\text{ }^{\circ}\text{C}$. We will need to determine the stability of our cavity experimentally to assess how far off and in what direction we have set the ULE's temperature. Doing this can help us optimize the frequency stability of our ULE system. Due to time limitations and other projects in the lab taking priority, we were unable to determine the short-term stability of the ULE at the time of writing this thesis. To determine the stability, we would need to prepare another ^{87}Rb one-photon Stark-shift experiment with the details laid out in Section 3.2. Thirty minutes of Stark-shift measurements at 3.5 Vcm^{-1} (or 10 kV across our 1.125'' wide field plates) should be sufficient to reveal the frequency stability of our ULE cavity at some set point of our temperature feedback circuit. The stability and frequency of the ULE cavity mode we use should also be measured annually to determine the aging of the system.

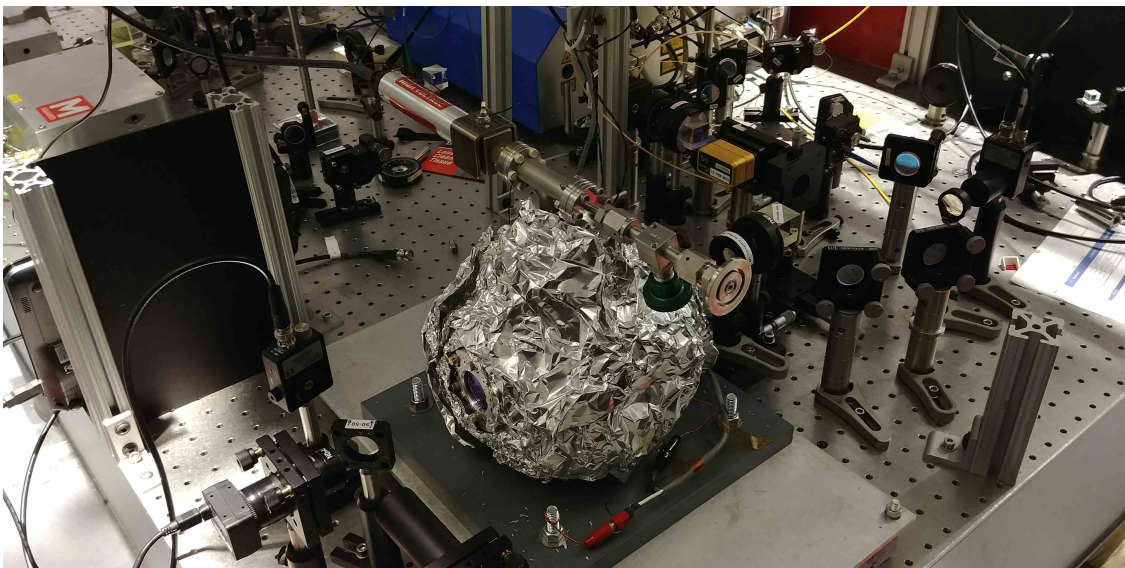


Figure 2.6: This is our ULE cavity vacuum system without the insulating shell. From this image we see the ion pump and high voltage cable on the far side above the vacuum chamber and a valve for a roughing pump on the near side. Other optics, photo-diodes, and our resonant electro-optic modulator is also visible on this bench.

2.1.3 PDH Locking Technique

This ULE cavity is used as a frequency reference in a new laser locking system to stabilize our probe laser. The design was based on the streamlined interpretation of the fast-modulation-PDH method developed by E. Black [14].

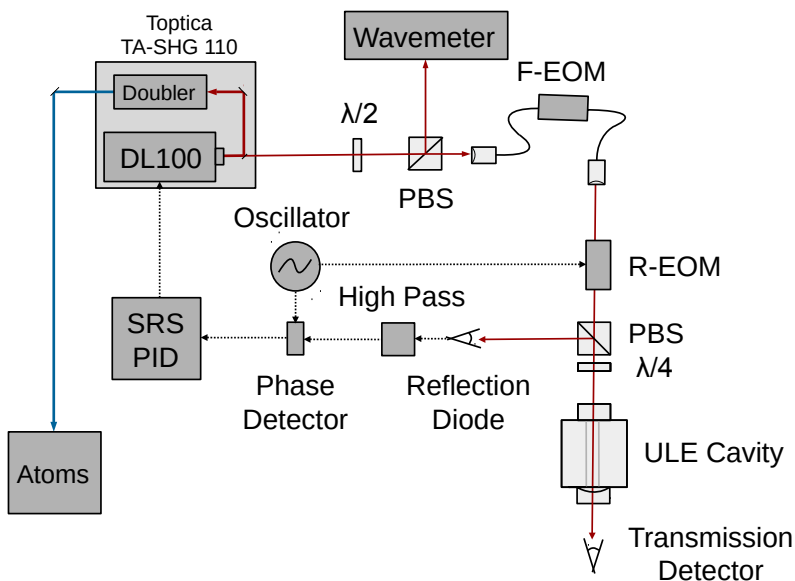


Figure 2.7: An illustration of the optical and electrical signals used in our double-electro-optic modulator (EOM) laser locking scheme for one-photon spectroscopy.

With our current setup illustrated in Figure 2.7, a Topica TA-SHG 110 unit produces the probe beam for our $5s \rightarrow 6s$ spectroscopy in Rb. The carrier frequency of this laser is set to 992 nm where we would otherwise use an M^2 laser set to 1012 nm for analogous spectroscopy in Fr. The frequency of the carrier will be doubled before being sent to our atoms for one-photon spectroscopy where we will lock a non-doubled pick-off light to the ULE cavity. The mirror coatings of the cavity were chosen to operate at 992 nm and 1012 nm for this reason.

We aim to use the pick-off light to produce a signal containing information about how far off and in what direction our probe laser has drifted with respect to our cavity, an error

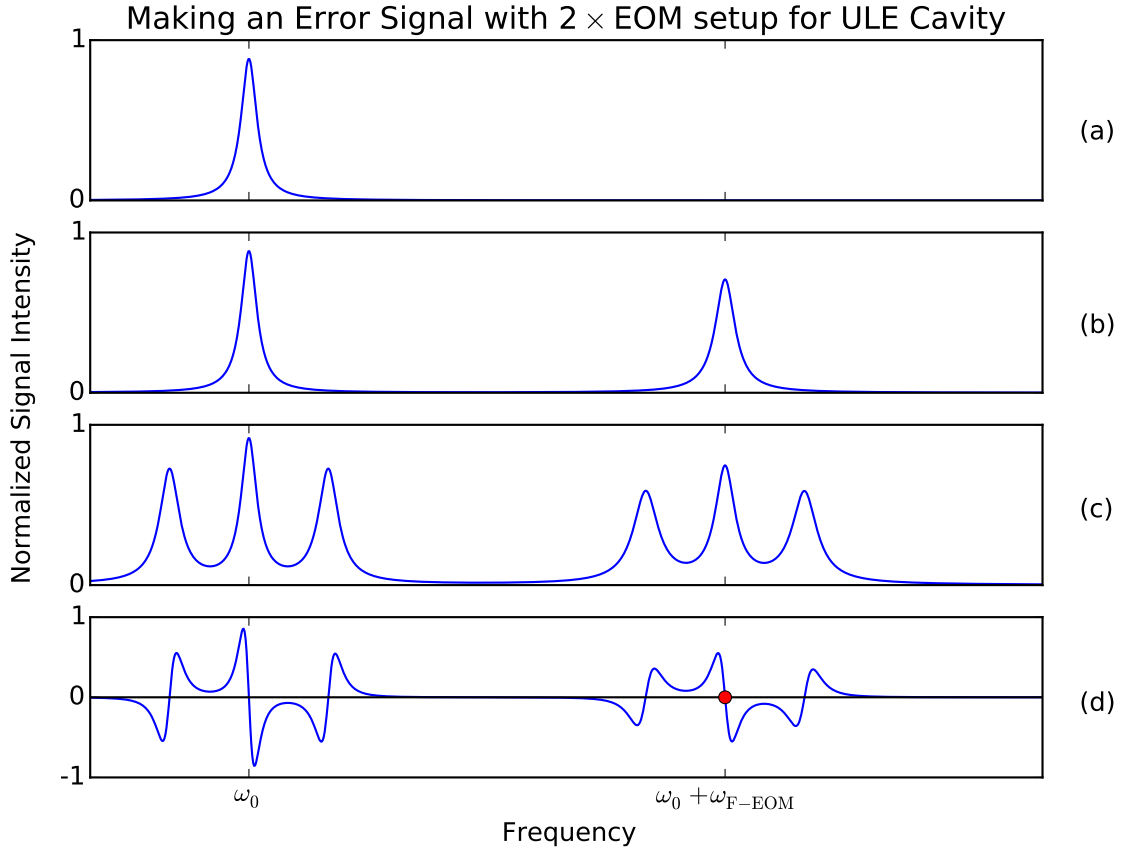


Figure 2.8: This is a model of how we produce our error signal. (a) First we have the carrier frequency ω_0 of the pick-off. (b) We modulate the light with our F-EOM to create a sideband resonant at our frequency of interest, $\omega_0 + \omega_{F-EOM}$. (c) We modulate the light again with our resonant electro-optic modulator (R-EOM) creating a second set of sidebands. (d) This light enters our cavity and reflects back into a fast diode where a comparison of phase of its output and the R-EOM results in the error signal. We would lock our cavity at the location of the red circle for our setup.

signal. Following Figure 2.8, the pick-off light is first sent through a fiber electro-optic modulator, or F-EOM (iXblue NIR-MPX-LN-20) [15]. This creates a set of sidebands with some frequency $\pm \omega_{F-EOM}$ away from the carrier frequency ω_0 up to 20 GHz for this particular model. We want to lock one of these sidebands to a lowest order transverse electromagnetic mode ($TEM_{0,0}$) of our cavity. This way, we can control a frequency scan over our atomic

resonances by controlling the modulation frequency of our F-EOM. The free spectral range of our cavity, or the frequency separation between subsequent $\text{TEM}_{0,0}$ modes we can lock to, was chosen to be 1.5 GHz, so we are not limited by the scanning range of our F-EOM. After the F-EOM, the pick-off-light is modulated again by a resonant electro-optic modulator R-EOM (New Focus 4001) creating another set of sidebands with frequencies $\pm \omega_{\text{R-EOM}}$ from the carrier and sidebands first created by the F-EOM, as modeled in Figure 2.8(c). After this second modulation, the pick-off-light is carefully coupled into the cavity and reflected back out into a fast photo-diode (Thorlabs PDA10CF 150 MHz) whose output will have its phase compared to the frequency modulation of the R-EOM with a phase detector (Mini-Circuits ZRPD-1+). The difference in phase results in an error signal resembling Figure 2.8 (d) at the output of the phase detector and input of our proportional-integral-derivative (PID) device. The frequency of a ULE cavity $\text{TEM}_{0,0}$ mode represented as a red circle in Figure 2.8 (d). If the frequency of the laser drifts above or below this frequency, our PID receives a negative or positive potential, respectively. Depending on the gain settings in place, this error signal is multiplied by some proportional gain value, integrated over some time, and has a derivative over some set time taken to predict future trends. The output of our PID is now a voltage potential that can correct frequency drifts of the probe laser. With our current setup, this potential is then sent to a piezo mounted behind a grating on a lever in the Toptica DL 100 laser within our TA-SHG 110 unit, as shown in Figure 2.9. Applying voltage to this piezo will change its size and the incident angle of a diode laser's light on the grating, resulting in small frequency changes of the laser's output. The potential supplied by the PID corrects the probe laser as to bring the middle of the error signal back to the frequency of the $\text{TEM}_{0,0}$ cavity mode. By locking a F-EOM sideband to our ULE cavity in this way, the frequency

stability of our spectroscopy laser can be improved up to the limit of the frequency stability of the ULE cavity itself.

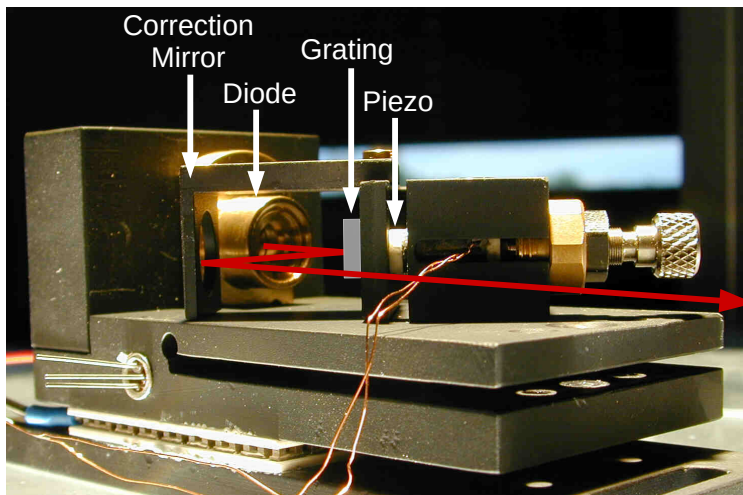


Figure 2.9: Exposed Toptica DL100 laser block. Original image taken and modified from the LARISSA group [16].

When scanning, we intentionally make small frequency steps in the F-EOM modulation frequency and expect the PID to quickly respond to this change without losing the lock. In effect, the absolute frequency of the F-EOM sideband is fixed allowing us to adjust the F-EOM modulation to scan the carrier frequency of our probe laser. Depending on the power and coupling efficiency of light through our ULE cavity, we are able to make frequency steps as large as 0.65 MHz at a time. This is partly limited by the linewidth of our cavity being 2.2 MHz. However, the amplitude of the sidebands produced by our F-EOM have been observed to change as much as 10% as a function of the modulation frequency. Our PID lock responds poorly to these signal intensity changes and can make locking impossible without reoptimizing our PID gain settings. We have been able to slowly scan a range as far as 65 MHz over five seconds with a hundred small steps of 0.65 MHz at a time. Total

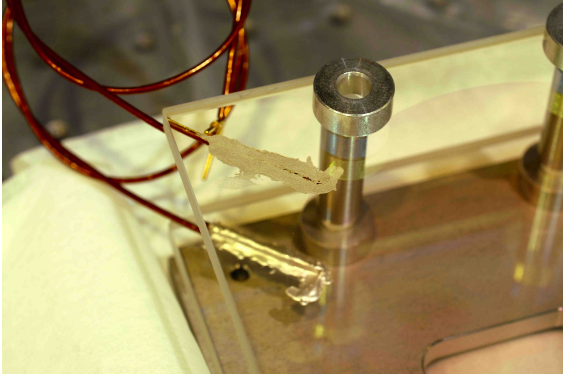
scans larger than 65 MHz or with steps larger than 0.65 MHz are prone to lose the PID lock because of this variable amplitude effect. More time needs to be spent characterizing the F-EOM's variable amplitude effects and optimizing the gain settings of our PID lock if we require scan ranges larger than these. At the time of writing this thesis, investigations are underway to optimize the frequency stability of the ULE and the locking stability of this system.

2.2 ITO Electric Field Plates

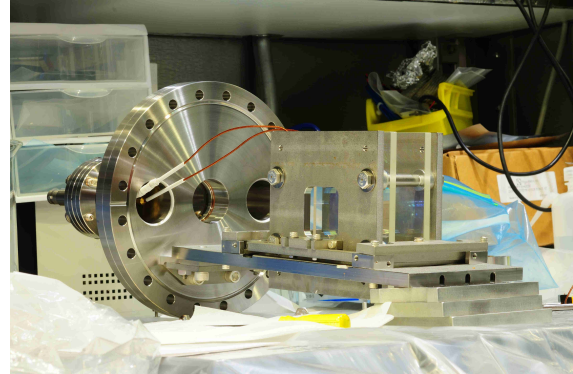
In our science chamber, we use electric field plates to cause Stark-shifting and Stark mixing in our alkali atoms. Applying an external electric field over our atoms causes shifts in atomic resonances which we can use to determine scalar and vector polarizabilities of our atoms. The second unique phenomenon of an applied external electric field is that electron states of different parity also become mixed in the presence of an external electric field. This allows the Stark-induced transition we want to stimulate in our future APNC measurements.

A recent development at the FTF was the installment of new glass (BK7) electric field plates coated with a conductive layer of indium-tin oxide (ITO) manufactured by Custom Scientific [17]. As shown in Figures 2.10, these transparent plates allow beams necessary for trapping to pass through while they sandwich a set of four stainless steel spacers. Each spacer (1.125" long, 303 Stainless Steel, 17.3 $\mu\text{m}/\text{m}/\text{K}$ [18]) has a 10 μm tolerance in length as listed by the manufacturer, Kager Industries. With a set of four spacers evenly placed around the plates, the total uncertainty in the plate spacing is reduced to 5 μm .

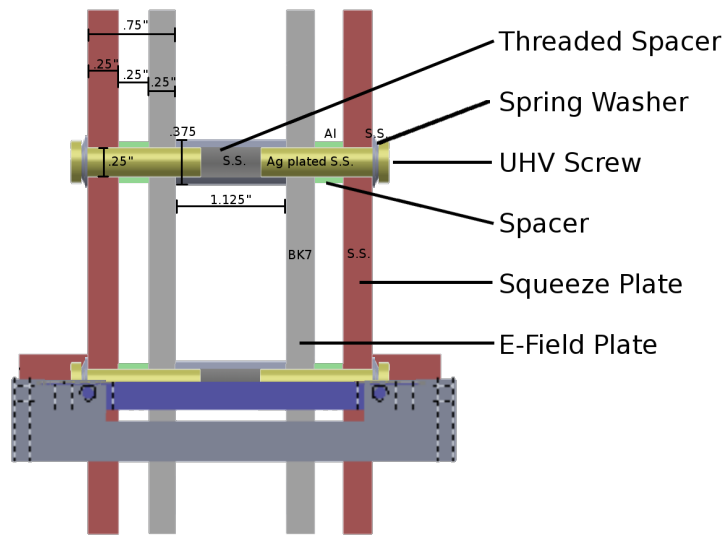
In practice, the plates have performed well up to 15 kV. Beyond this limit, we observe our high voltage supply (Stanford Research Systems Model PS375) trip indicating that arcing has taken place. These plates are being used in current measurements and have been used in preliminary observations described in Chapter 3.



(a)



(b)



(c)

Figure 2.10: (a) We used a conductive epoxy to bond leads to the inner indium tin oxide (ITO) coatings of our field plates. (b) ITO plates in our ‘sandwich’ assembly before being installed in our primary science vacuum chamber. (c) A model of the cross section of our sandwich assembly indicating how it is held together with bolts, spacers and washers.

Chapter 3

Spectroscopy

Aside from its instability and radioactivity, spectroscopy in francium is challenging because the $7s \rightarrow 8s$ transition was never directly observed previously. The $8s$ state has been stimulated from $7p$ state, which has given us insight as to the frequency of this direct transition [19]. In August 2016, we performed parity-allowed two-photon spectroscopy for this transition in several isotopes of francium [9]. In November of the following year, we were able to try out our ULE locking technique for the first time and collect preliminary data to give us a clue of what ^{87}Rb one-photon Stark-shift measurements may look like.

3.1 Fr $7s \rightarrow 8s$ Two-Photon

The August 2016 beamtime for the Francium Trapping Facility (FTF) allowed us to directly observe the parity-allowed, same-frequency, two-photon $7s \rightarrow 8s$ transition for the first time in isotopes $^{208-211}\text{Fr}$ and ^{213}Fr [9]. Measuring the frequency of these transitions combined with previous studies of the $7s \rightarrow 7p_{1/2}$ transition allowed us to perform a King plot analysis [20]

to determine the ratio of the field shift constants from the relationship

$$\frac{M_A M_{A'}}{M_A - M_{A'}} \delta\nu_{IS,D1} = \frac{F_{D1}}{F_{SS}} \frac{M_A M_{A'}}{M_A - M_{A'}} \delta\nu_{IS,SS} + (N_{D1} + S_{D1}) - \frac{F_{D1}}{F_{SS}} (N_{SS} + S_{SS}) \quad (3.1)$$

where $N_{D1}(N_{SS})$, $S_{D1}(S_{SS})$, and $F_{D1}(F_{SS})$ are the normal mass shift, specific mass shift, and the field shift of the D1(7s→8s) transition. This type of analysis results in a purely electronic observable which is a good gauge as to the ability of the many-body calculations to describe the francium atom at a level necessary for the interpretation of future APNC measurements.

As described in the introduction, we began our experiment by capturing and neutralizing a beam of francium ions, then performing a cold transfer to our science chamber. We tune our trapping and repumping lasers depending on the specific isotope we are studying. An M² SolsTIS Ti:Sapphire laser was used at 1012 nm to produce the probe beam to excite the 7s→8s transition between both upper hyperfine s-states as shown on the right of Figure 1.3. The frequencies of our trapping, repumping, and probe lasers were all locked to a stabilized HeNe laser with a computer controlled feedback system [8]. For this two-photon scheme, 350 mW of linearly polarized probe laser light was focused over our 1 mm³ trap of francium. This beam is re-collimated, reflected, and refocused back on the trap to increase its intensity at the atom cloud.

With the locking scheme in place at the time, a pick-off beam from our probe laser was modulated with an acousto-optic modulator (AOM) in double-pass configuration, then locked to our HeNe laser. Slowly ramping the modulation frequency of our AOM causes the lock feedback to compensate by ramping the carrier frequency of the probe laser; the modulated pick-off frequency remains unchanged in this setup. During this beam time, our

probe laser scanned 37.72 MHz over the $7s \rightarrow 8s$ resonance. After being excited to the $8s$ state, the single valence electron would rapidly decay through the $7p_{1/2}$ or $7p_{3/2}$ state and back to the ground state. Because we trap with the D2 line ($7p_{3/2} \rightarrow 7s_{1/2}$ at 718 nm), we could only use observations of the D1 line ($7p_{1/2} \rightarrow 7s_{1/2}$ at 817 nm) to indicate that we were resonant with the $7s \rightarrow 8s$ transition. A PMT below our science chamber would count the 817 nm photons while we scan our probe beam over our MOT. The PMT collects photons during several repeated scans where the photon counts are summed together and logged in a text file. An edge filter (Semrock LP02-785RU) and a long pass filter (Thorlabs FGL780RU) were installed before the PMT to significantly reduce noise from our trap light. To further reduce the noise and effects of the AC Stark-shift in our data, trap light was cycled on and off during scans where data was collected during the 1 ms off period.

Figure 3.1 shows an accumulation of ten scans at 12 s a piece using this two-photon excitation technique in ^{211}Fr with a bin separation of 157 kHz. M. Kalita fitted a Voigt function with an exponential decay over the data using the program MINUIT in ROOT to find the frequency of the fluorescence peak. The short 14 ± 3 second lifetime of the trap ($1/e$) made it necessary to include this exponential decay in the fitted models where the resulting fitted models did not significantly deviate from the data at the 5% significance level. The center of gravity (C.O.G.) for the $7s \rightarrow 8s$ transition was determined in each of the five isotopes studied with an error of 2 MHz. Isotope shifts were then determined by subtracting the C.O.G. of this transition in ^{213}Fr from the C.O.G. of the same transition in the other four isotopes.

With this information, we were able to perform a King plot analysis where the isotope shifts of the $7s_{1/2} \rightarrow 7p_{1/2}$ transition are plotted against the isotope shifts of the $7s_{1/2} \rightarrow 8s_{1/2}$

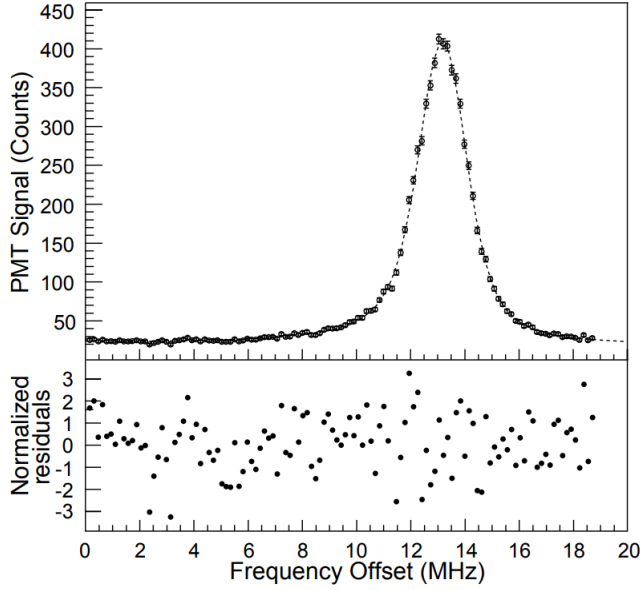


Figure 3.1: Typical two-photon spectroscopy data for our scan over the $7s(F=5) \rightarrow 8s(F=5)$ transition in ^{211}Fr . The bottom plot shows the normalized residuals for the fitted Voigt and exponential decay functions seen as a dashed line over the primary plot. Data reduced by M. Kalita [9].

transition which should produce a straight line from *ab initio* theory. The results of this plot are shown in Figure 3.2 where the slope of the fitted line (ratio of field shift constants)

$\frac{F_{D1}}{F_{SS}} = 1.228 \pm 0.019$ is in excellent agreement with the theoretical value of 1.234 ± 0.019 .

These results will help us interpret future APNC measurements.

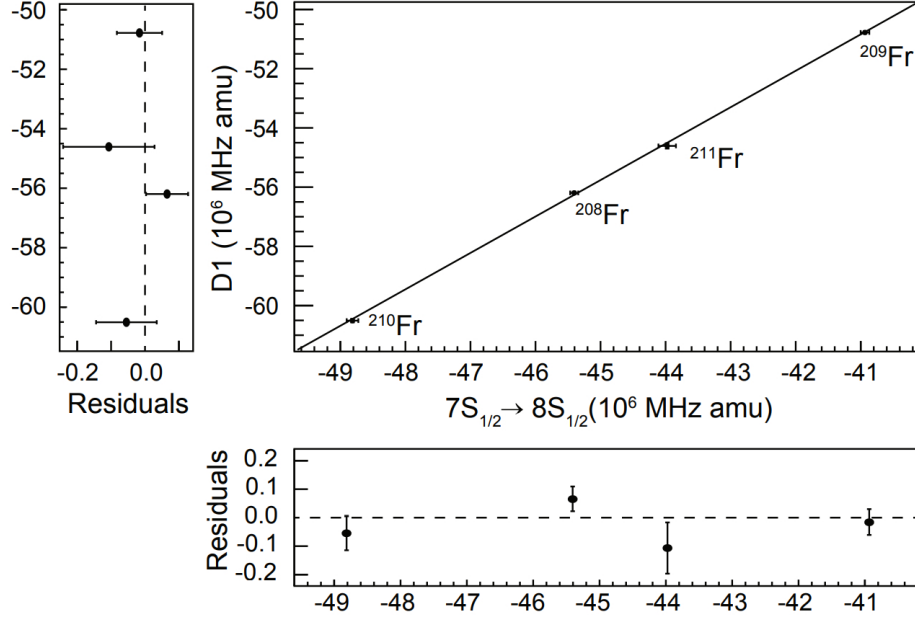


Figure 3.2: Isotope shifts of the D1 line against the $7s \rightarrow 8s$ transition for isotopes $^{208-211}\text{Fr}$ and ^{213}Fr . Data reduced by M. Kalita [9].

3.2 Rb $5s \rightarrow 6s$ One-Photon Stark-Induced

The next step for our collaboration is to excite the $8s$ orbital in francium with a parity-allowed, one-photon, Stark-induced transition directly from the $7s$ ground state. To prepare for this measurement, we experiment with one-photon stimulations of the analogous transition in rubidium as illustrated in the left of Figure 1.3.

3.2.1 Theory for DC Scalar Polarizability Measurement

We want to identify potential issues we may run into for future Stark-shift measurements, so we have performed a new auxiliary investigation of the atomic polarizability for the $5s \rightarrow 6s$ transition in ^{87}Rb . Scalar polarizability, α , describes the tendency of the single valence

electron cloud in our alkali atom to be displaced by a static external electric field [21]. Each electron state will have its own value for polarizability, so our Stark-shift investigation will reveal the *change* in polarizability between the $(n + 1)s$ and ns orbitals, $\Delta\alpha$ [22]. Because we have chosen a trapping scheme that discourages electrons of our atoms from populating the lower hyperfine state of our ns orbital, we will be probing the upper hyperfine states for the $ns \rightarrow (n + 1)s$ transition. For ^{87}Rb , we will probe the single-photon $5s_{1/2} F = 2 \rightarrow 6s_{1/2} F = 2$ transition.

The energy levels of electron states within an atom will be perturbed by an external electric field as a function of the square of the magnitude of an applied electric field $|\mathbf{E}|$ and the scalar polarizability of that state α :

$$\Delta E = -\frac{1}{2}\alpha|\mathbf{E}|^2. \quad (3.2)$$

This investigation probes electron excitations from the ns orbital to the $(n + 1)s$ orbital in our alkali atoms and how the frequency of the photons responsible for the transition, ν_{Stark} , changes with the applied electric field. In our science chamber, we have an effective parallel plate capacitor about our atomic sample with some fixed distance, d , and variable voltage, V , across the plates. These measurable quantities relate to each other by

$$\nu_{\text{Stark}} = k \frac{V^2}{d^2} \quad (3.3)$$

with some Stark-shift constant, k , in $\text{kHz cm}^2 \text{ kV}^{-2}$. Following the conventions of S.C. Bennett [23] and M.S. Safronova [24], it follows that k is related to the scalar polarizability

by

$$k = \frac{\Delta\alpha}{2} \frac{4\pi\epsilon_0}{h}. \quad (3.4)$$

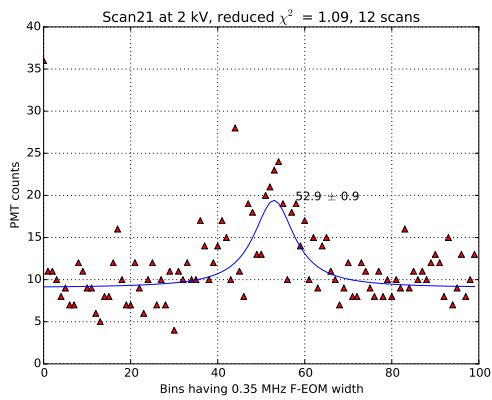
with Plank's constant, h , and the vacuum permittivity constant, ϵ_0 , where $\Delta\alpha$ is usually stated in atomic units.

3.2.2 Parameters and Results of Experiment

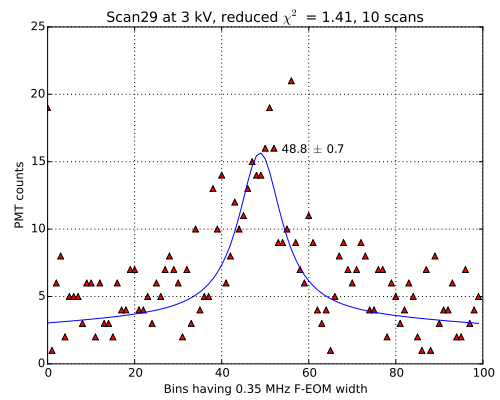
Preliminary data has been taken to examine the change in scalar atomic polarizability between the 5s and 6s states in rubidium while being perturbed by electric field strengths up to 4.5 kVcm^{-1} resulting in Stark-shifts up to 14 MHz.

To take this data, we used a similar chopping-scanning technique performed in our francium two-photon investigations. As described in Section 2.1.3, our Toptica TA-SHG 110 laser produces a 992 nm primary beam to be doubled in frequency to 496 nm and sent to stimulate our atoms while a pick-off from the primary beam is modulated by our F-EOM and a resulting sideband is locked to the ULE cavity. With some electric field set across our atoms, we would count photons and sum the bins from a series of forward scans resulting in the plots shown in Figure 3.3.

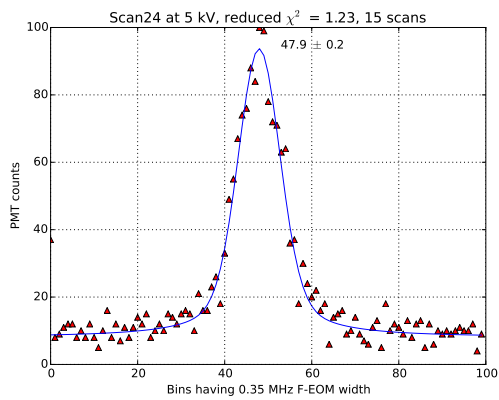
Recall that the pick-off beam we lock is not doubled. Because of this, a 1 MHz shift in our F-EOM results in the doubled light to the atoms shifting by 2 MHz which is an effect we are careful to remember in our later analysis. With this locking scheme in place, multiple scans taken at specific potentials were summed to improve the signal-to-noise of the set. Next, the Python port of the CERN fitting software MINUIT was used to fit a Voigt function with an offset over the data. The fitted functions were determined to have a reduced χ^2 between 1 and



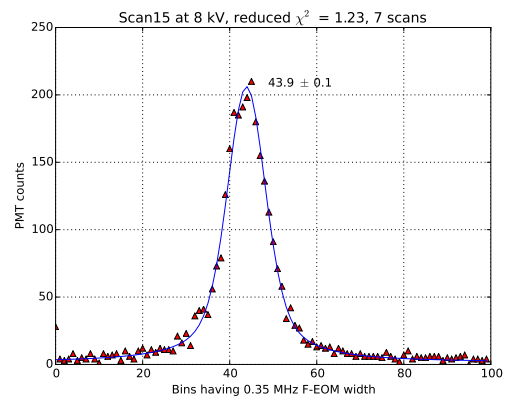
(a)



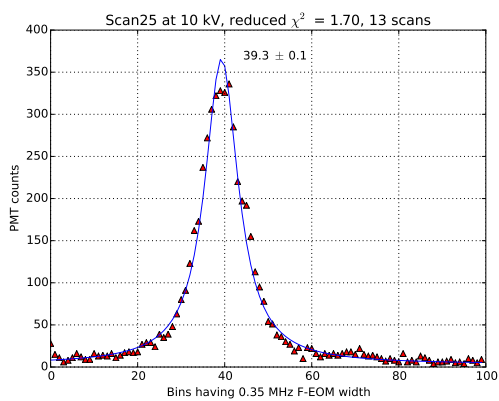
(b)



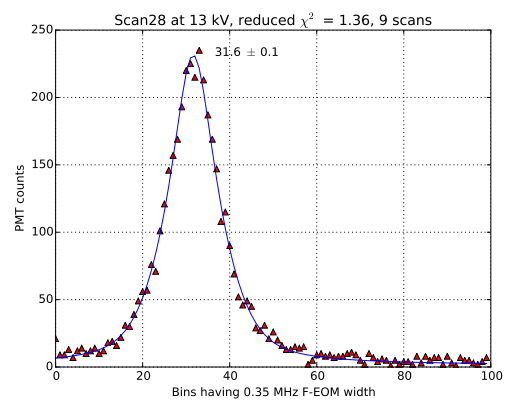
(c)



(d)



(e)



(f)

Figure 3.3: Each image shows the sum of a set of scans during a first quick check of a ^{87}Rb Stark-shift measurement on 7-Nov-2017. The bin positions of the centroids for this Voigt fit are converted to frequency and used to produce the results in Figure 3.4(a).

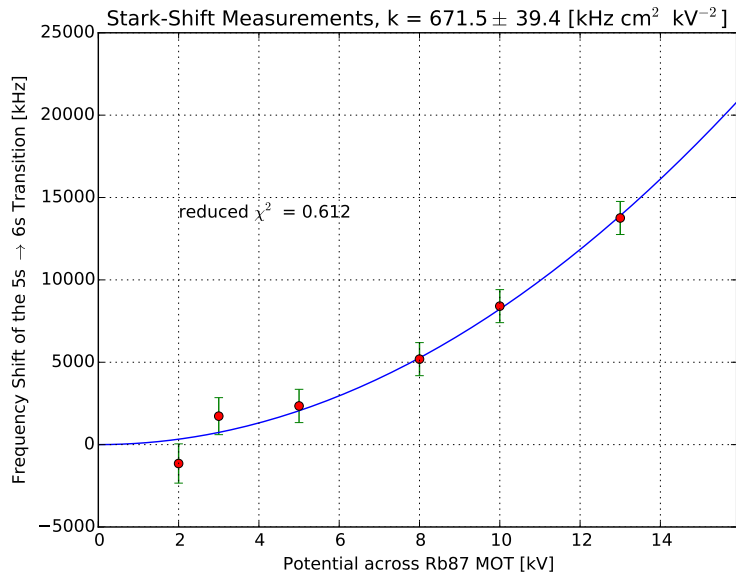
2 suggesting the models do not significantly deviate from the data. The fitting software then reports the bin and of the centroids along with the error associated with the bin position. The frequency spacing of the bins is known and we can extrapolate the frequency of the 5s→6s resonance relative to similar measurements at different potentials. It is important to note that the Stark mixing that enables this transition is significantly reduced at low applied external electric fields. Because of this, the errors in the centroid become large at low potentials as we would expect. At the time of taking this data, inconsistencies in frequency measurements as large as 1.5 MHz were observed and not fully understood. For this reason, an error of 1 MHz is added in quadrature to the centroid errors for all of our data points. The centroids and total error of the centroid are converted to frequency and put in a scatter plot, shown in Figure 3.4(a).

Using MINUIT again, we find the best fit of the experimentally determined Stark-shift constant k_{exp} for mapping equation 3.3 onto our scatter plot. The reduced χ^2 of this fit came out to 0.612 which suggests we can improve the uncertainty in our peak positions with future measurements. When MINUIT minimized our reduced χ^2 for our Stark-shift analysis

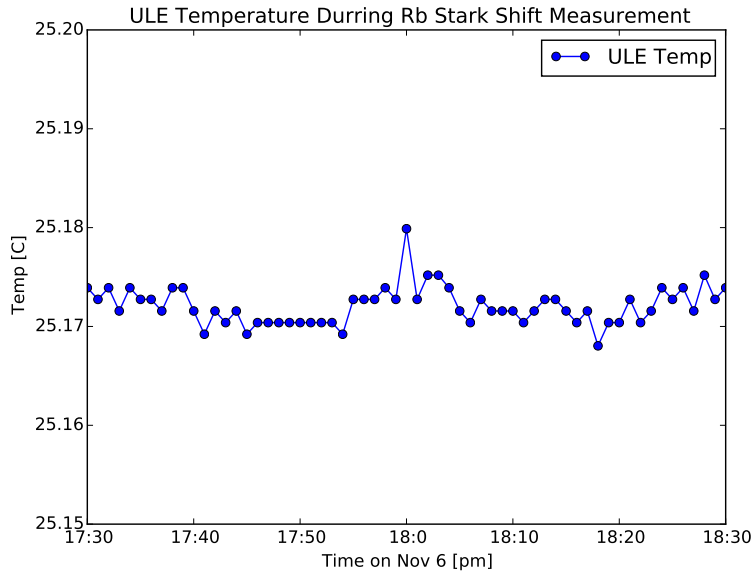
$$\text{Reduced}\chi^2 = \frac{\sum_{\text{for all } i} \left(\frac{\text{real}[i] - \text{model}[i]}{\sigma_{\text{real}}[i]} \right)^2}{i - 2}, \quad (3.5)$$

we weighed data by the variance of the real data points, $\sigma_{\text{real}}[i]^2$, being one standard deviation of our centroid bin squared. With the large 1 MHz error included in σ_{real} , the combined error in our centroid positions resulted in our calculation of a predictably smaller reduced χ^2 .

For this analysis, our Stark-shift coefficient worked out to be $k_{\text{exp}} = 671.5 \pm 39.4$ kHz $\text{cm}^2 \text{ kV}^{-2}$. Additional data could not be collected due to our collaboration shifting focus to



(a)



(b)

Figure 3.4: Rubidium one-photon Stark-shift data while using the new ULE cavity to lock our scanning laser. The raw data from our temperature monitor indicates there was no greater than a 12mK temperature change during the measurement.

updating neutralizer equipment, updating our trapping schemes due to a pump laser failure, and recovering the ULE cavity locking system after two power outages. For these reasons and the included 1 MHz discrepancy we accounted for, this measurement serves as a test of our ability to collect data with our new device and stands apart from the theoretical prediction.

The literature predicts $\Delta\alpha$ to be 4854.1 a.u. with an uncertainty of 0.3% [22, 24]. This value works out to be 603.93 ± 1.8 kHz cm² kV⁻² after being converted to SI units through Equation 3.4. Our measured value of k_{exp} strays from this theoretical value by two standard deviations, though it is reassuring that both values are in the same ballpark.

3.2.3 Projecting Minimum Error in Scalar Polarizability

The determined value of $\Delta\alpha$ from the analysis in Figure 3.4(a) resulted in a fractional uncertainty of 0.5% although it will be useful to know the theoretical limit of how well future Stark-shift coefficients could potentially be measured. From Equation 3.3, the lower limit of the error in k (and subsequently $\Delta\alpha$) depends on the combined uncertainties of ν_{Stark} , d , and V where

$$\left(\frac{\sigma_k}{k}\right)^2 = \left(\frac{\sigma_{\nu_{\text{Stark}}}}{\nu_{\text{Stark}}}\right)^2 + 2\left(\frac{\sigma_d}{d}\right)^2 + 2\left(\frac{\sigma_V}{V}\right)^2. \quad (3.6)$$

As stated before, further studies need to be done to precisely determine the frequency stability of the ULE cavity where this directly affects the stability of the laser probing this transition. To get a very rough approximation of $\sigma_{\nu_{\text{Stark}}}$, let us assume our ULE cavity has a similar performance to the one studied by J. Alnis [10]. For very small temperature

changes near the zero crossing temperature, frequency drift becomes linear with temperature. From his work, a ULE cavity's temperature maintained $\pm 0.5^\circ\text{C}$ away from the zero crossing temperature results in a frequency stability of 300 Hz/mK. During our hour long experiment, the ULE was reported having a temperature standard deviation of 2 mK. From this, we can make the conjecture that $\sigma_{\nu_{\text{Stark}}} = 600$ Hz. If we make scans with a resolution on the order of 0.70 MHz, as we have in Figure 3.3, then the fractional uncertainty of our frequency comes out to $\left(\frac{\sigma_{\nu_{\text{Stark}}}}{\nu_{\text{Stark}}}\right) = 0.00086$.

Our electric field plates are separated by a set of four custom stainless steel spacers with lengths $1.125'' \pm 0.0004''$ as declared by the manufacturer, Kager Industries. Here we assume the lengths are statistically scattered, although it is more likely that one machine was used to cut our spacers which is more likely to produce a systematic offset. Given that the spacers are evenly spaced about the field plates, the combined error in the distance of the plates falls by a product of one over the square root of the number of spacers, so $\sigma_d = 0.0002''$. The fractional uncertainty of the distance rounds out to be $\left(\frac{\sigma_d}{d}\right) = 0.0002$.

Lastly, we use a Stanford Research Systems (SRS) model PS375 power supply to generate the potential across our field plates. The fractional uncertainty of the set voltage for this unit is $\left(\frac{\sigma_V}{V}\right) = 0.0006$, taken from the user manual [25]. The manual also expresses there is no way for the user to verify the on-board calibration and does not express how the calibration changes with aging, so this error is taken as conjecture for now but will be verified by a high voltage probe in the future.

In total, the fractional uncertainties of our variables combine in equation 3.6 making the lower limit in the total fractional uncertainty of k and $\Delta\alpha$ to be 0.12%. If the previous conjectures could be experimentally verified and result in similar fractional uncertainties,

future official measurements of k and $\Delta\alpha$ can have competitive values compared to the established theoretical values [22].

More efforts need to be made to establish the uncertainty limits of our setup and to finish a thorough determination of $\Delta\alpha$. Once we are confident in our methods and analysis, we will be ready to pursue analogous measurements in francium.

Chapter 4

OUTLOOK

The goals of the FTF will keep students and collaborators busy for years to come. It seems maintaining the intricate array of equipment in the lab takes as much effort as developing new systems for future measurements, if not more. The new ITO electric field plates are sufficient for our short and medium term goals. This feeling is motivated by our confidence in the separation of these plates.

The construction and early development of the ULE cavity was the primary focus of my research while at TRIUMF. Though construction is complete, more effort needs to be spent quantifying the performance of the system. The stability of the system performs best when the set temperature is the same as the zero crossing temperature of the ULE. Unfortunately, we have large uncertainty in our measured zero crossing temperature and potentially an equally large systematic uncertainty in our temperature measuring device, therefore it will take some time to adjust the temperature of the ULE cavity to optimize the frequency stability of the system.

Maintaining optical alignments and pump pressure of the ULE have also revealed design

flaws in the ULE cavity project. Power outages or lab mishaps that cause our ion pump to shut off for too long result in the vacuum pressure deteriorating to the point where roughing down the pressure is required. To do this, the insulating shell needs to be removed to gain access to a roughing pump valve. The cavity rests on a different (and less solid) platform than the rest of the optics that send light into the cavity, so misalignments readily occur while removing the shell or even attaching plumbing for our roughing pump. After pumping and re-installing the shell, it is usually a two-day job to re-align light through the ULE cavity and to optimize the error function for the laser lock. We hope to prevent future accidental shutdowns of the ion pump by implementing an uninterruptible power supply, but future students will need to become familiar with the setup and the process of getting the ULE cavity and R-Pi operational in the event of a lab shutdown.

The mirrors of the ULE cavity were also selected to be functional at 780 nm, making it possible to upgrade the system by locking our trap and repump lasers to the cavity if the opportunity arises.

Future students in the lab will also need to familiarize themselves with how we lock our scanning lasers to the ULE cavity as it is required for the spectroscopy at the heart of our research. We have only begun to investigate DC Stark-shifts but work still needs to be done to determine the uncertainties of frequency and potential in our setup. Once we do this, we will be prepared for analogous measurements in francium and proceed with other objectives on the way to a PNC measurement.

Appendix A

IGBT Current Switch Board

During future APNC measurements, we will want to spin-polarize our francium atoms, but the presence of our trapping anti-Helmholtz coils will mix m -states, adding another layer of difficulty to the experiment. A solution we have considered implementing is ‘chopping’ our MOT: briefly turn off the light and fields required to trap atoms, take data, then resume trapping with the light and fields. In practice, chopping will take place hundreds of times while we scan over atomic resonances of our samples, so it is important that the duration of each chop is short enough that we do not lose a significant number of atoms. In our rubidium Stark-shift investigations, we have chopped just the laser light with a duration of 5 ms resulting in a reasonably small loss of trapped atoms. Of those 5 ms, we take data for 2.8 ms, so we will require a device that will quickly stop and restart current flowing to our MOT coils with a switching time below 1 ms.

IGBT Design

A high current switch board utilizing insulated-gate bipolar transistors (IGBTs) is in development to help us with our future spectroscopy goals. Previously, current from a power supply directly flowed through our MOT coils. Now the power supply is connected to the prototype IGBT board where current can be switched back and forth from the MOT coils to a resistance matched $33\text{ m}\Omega$ ‘dummy’ load on the board where these states are illustrated in Figure 4.1. With this board, we hope to make benchmark measurements to determine how quickly we are able to switch the current and shed light on other design concerns we may run into.

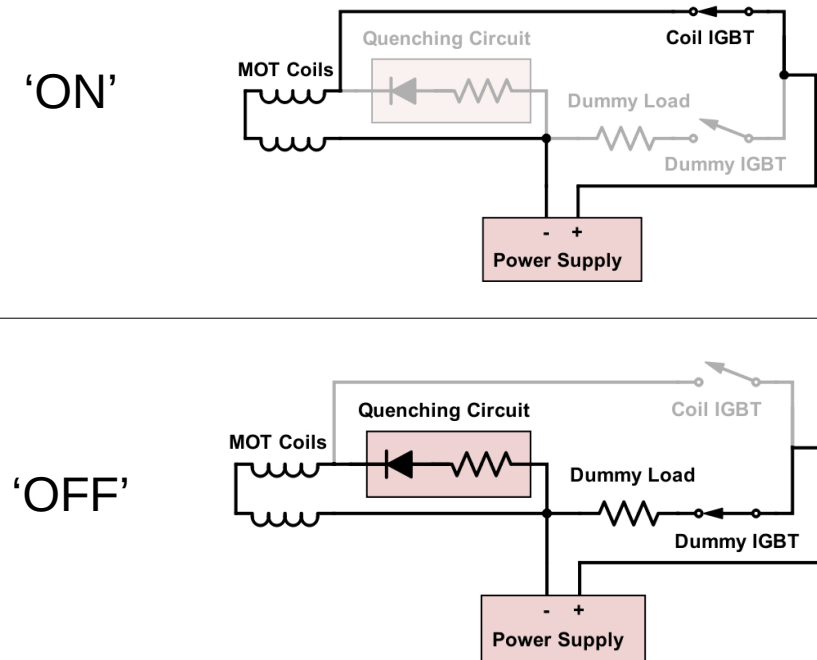
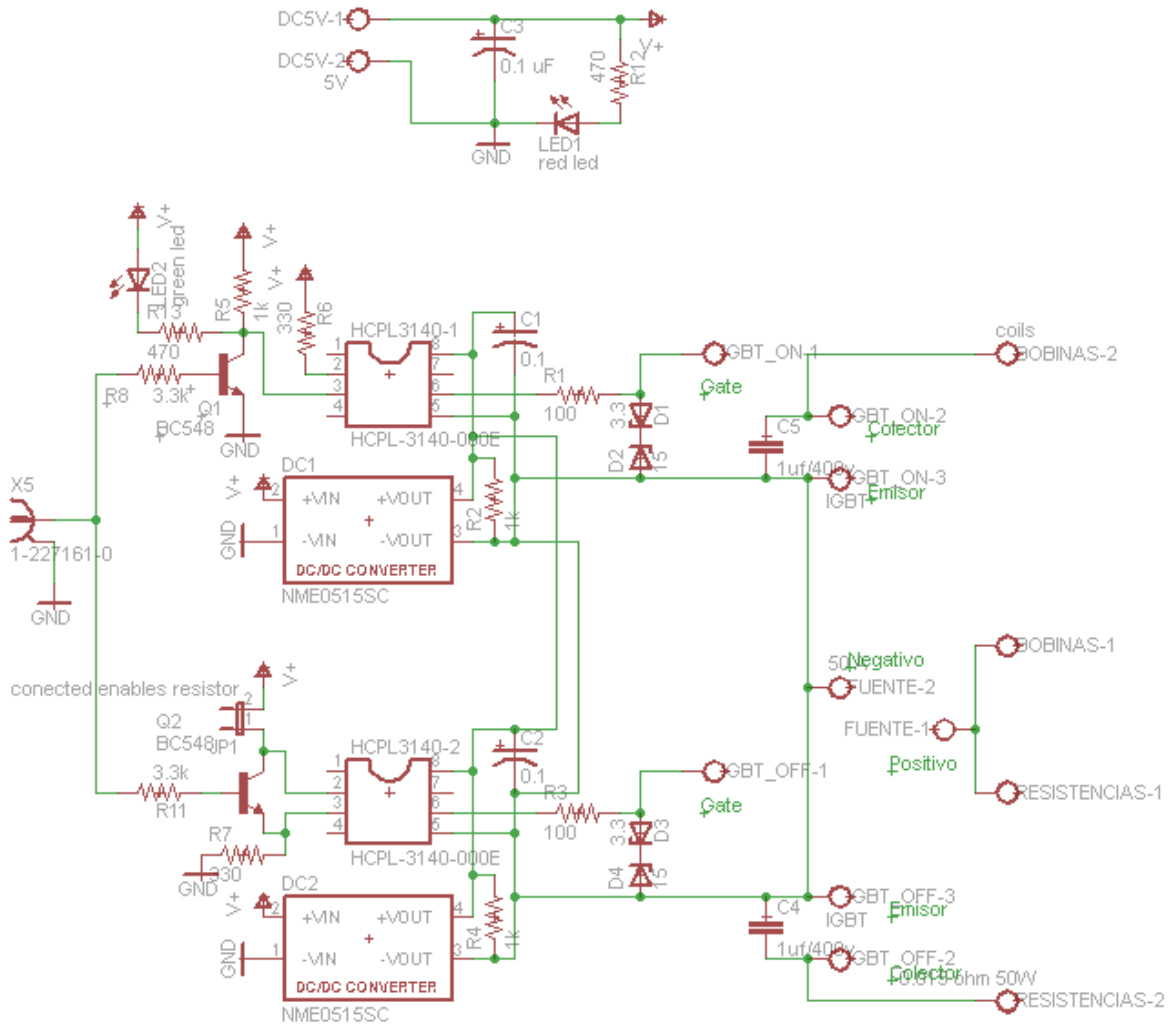
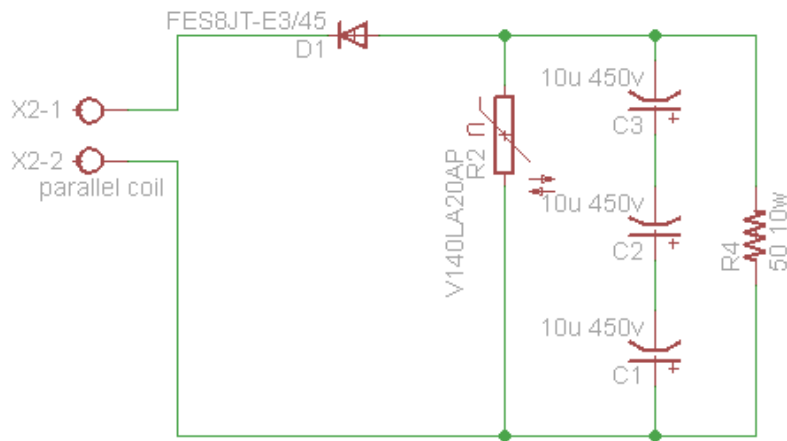


Figure 4.1: IGBT circuit in ‘on’ and ‘off’ configurations.



(a) Main IGBT circuit board.



(b) Coil quenching circuit.

Figure 4.2: IGBT switch and circuit schematics developed by E. Gomez.

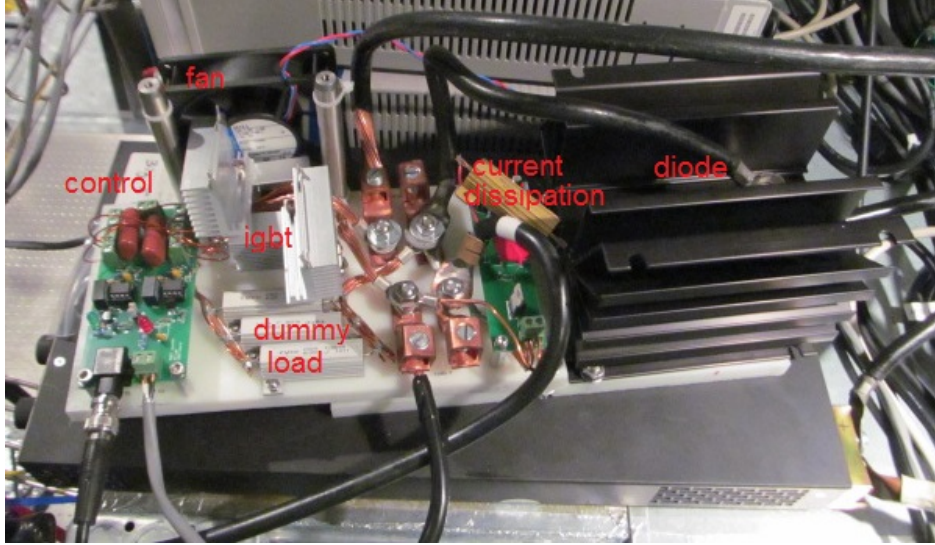


Figure 4.3: Prototype of the IGBT switch.

Early designs of our insulated-gate bipolar transistor (IGBT) switch were developed and constructed by E. Gomez, as shown in Figures 4.3. There are two IGBT chips on the switch, one for directing current to the local dummy load and the other for directing current to an external load [26]. When 6 V is applied across the gate and emitter of an IGBT chip, current is allowed to flow through it and its respective load where it would have otherwise behaved as a resistor. A central circuit board was developed to apply this voltage to one of the IGBT chips at a time depending on an incoming transistor-transistor logic (TTL) signal, as shown in 4.2(a). This TTL effectively sets this circuit in an ‘on’ or ‘off’ configuration as shown in Figure 4.1.

When in the ‘on’ configuration, current simply flows from the power supply, through the ‘coil IGBT’, to our MOT coils, and back through the switch to the power supply where the ‘dummy IGBT’ is set to behave as a resistor preventing current from flowing to the dummy load. In the ‘off’ configuration, the two IGBT switches change their states; current is directed through a resistive dummy load on the board while the remaining energy in the

coils is directed to a secondary quenching circuit that was previously inaccessible through a reverse biased diode, as shown in Figures 4.2(b) and 4.1.

IGBT Performance

We have tested how the IGBT interacts with two power supplies and our 162 μH , 32.1 $\text{m}\Omega$ science chamber coils. The original intention was to use our grounded Kepco (ATE 6-100M) power supply, but voltage spikes induced during switching caused a safety circuit to shut it off whenever current was set greater than 10 A. We had better luck working with a floating Sorensen (DLM 8-75) unit set to 50 A in constant current configuration. Taking care to avoid ground loops, potentials across local and external loads, as well as across our power supply, were measured with a scope during a 20 ms duty cycle for three different trials, as shown in Figure 4.4. The results of these trials are seen in Figure 4.5.

In our first trial (\circ), the IGBT was set to switch 50 A of current between two local resistive loads of 33 $\text{m}\Omega$. Current was observed to ring in the exterior load while interacting with the quenching circuit but leveled out after 100 μs . All other voltage transients were visibly suppressed within 50 μs . These switching times are excellent, but do not reflect how the board interacts with the cables leading to the coils and the coils themselves.

In the next trial (\square), the exterior resistive load of the IGBT was installed in series with approximately 15 m of 2/0 AWG cable. This is the cable normally used to run current to and from our science chamber coils. Voltage spikes occurred while directing current to the exterior load as before but transients were not sufficiently suppressed until after 2 ms. Directing current away from the exterior load again resulted in ringing that lasts 100 μs .

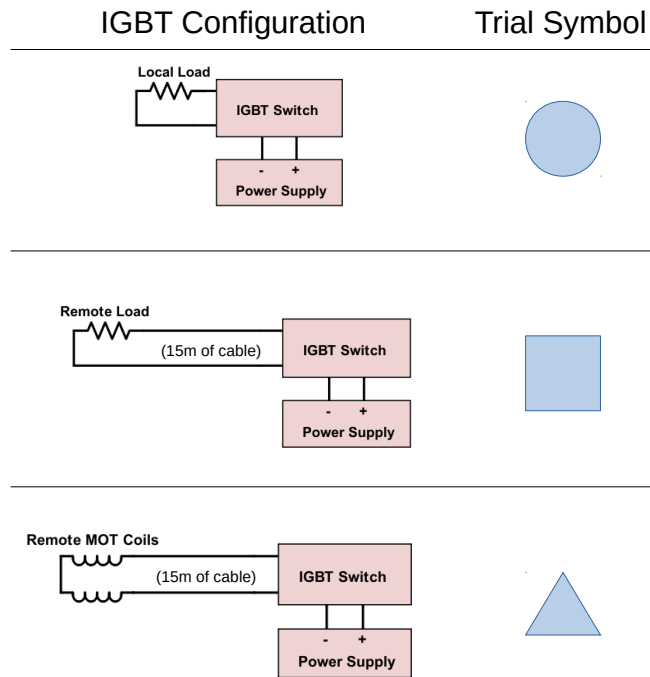


Figure 4.4: Configuration for three trials to test the performance of our IGBT circuit.

The cables in our setup along with the IGBT board present non-ideal behavior for restoring a MOT.

Lastly, the exterior resistive load was replaced with our MOT coils (Δ). We observed the potential across the inductive load to double as the inductive load began to charge in the initial 3 ms before tapering back to normal levels after 40 ms. Directing current away from the coils also caused a large kick-back of current which leveled off after 5 ms. This behavior is far from how we ideally want our IGBT board to perform with our MOT coils.

While trapping, we will want to drive our science coils with 75 A, so the amplitude and duration of the observed undesired transients in this trial will likely be amplified under its current configuration. We may need to include capacitors in the circuit to decrease the charging time of the coils when switched to the ‘on’ configuration. Under its current

configuration, the IGBT board is not suitable to act as a current switch for our MOT coils under the time-constraints required by future M1 spectroscopy.

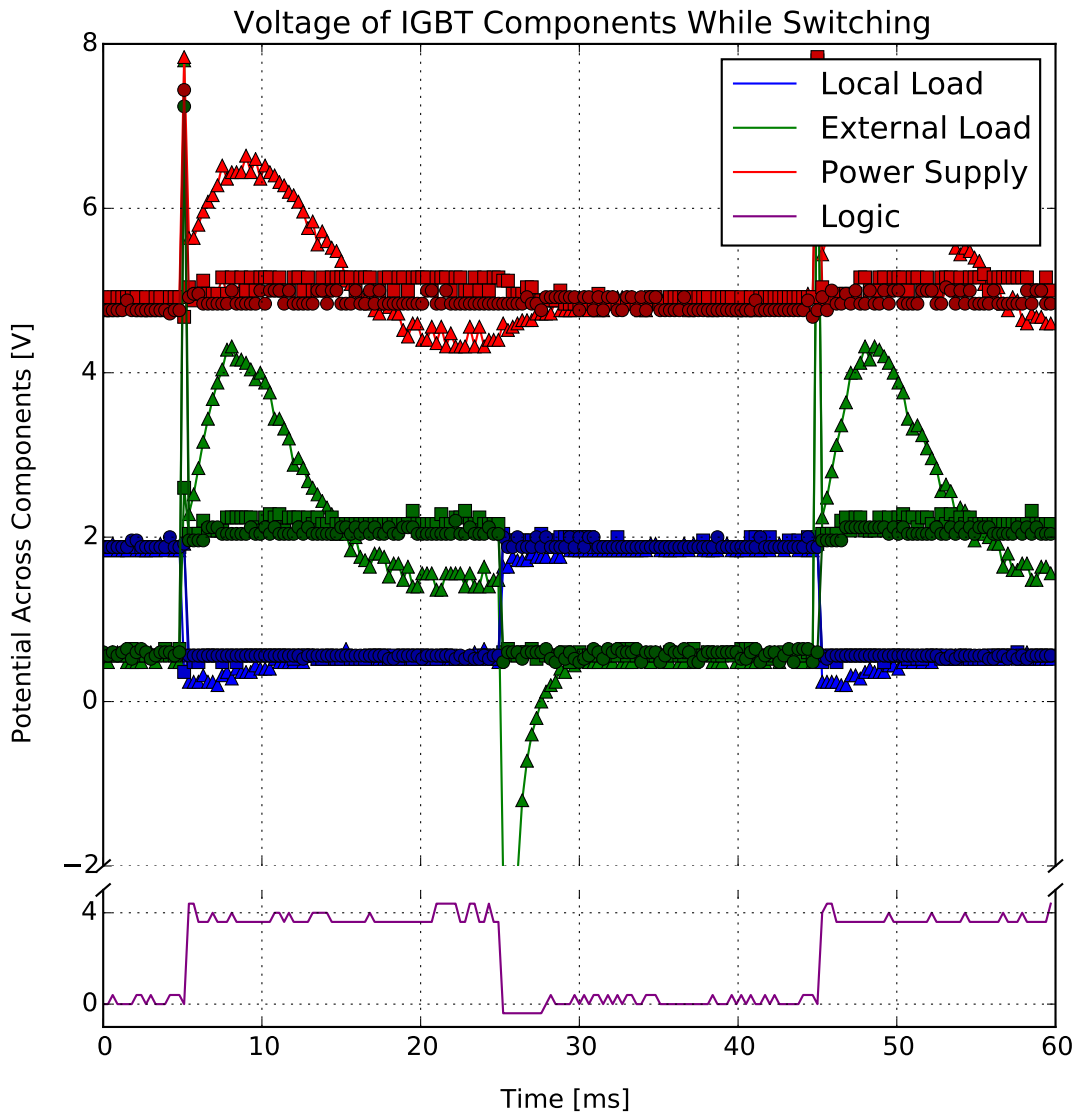


Figure 4.5: We want the IGBT board to switch current on and off to our magnetic field coils. Here we measure potential across different components on our IGBT setup for three trials of different external inductive loads. The circle, square, and triangle sets show data when current switches from the local resistive load to an external local resistive load, remote resistive load, and remote inductive load respectively. Below is a purple signal indicating the potential of our TTL which initiates the IGBT switching process.

Appendix B

Pneumatic Rotator and Foil Upgrades

As described in the introduction, the ISAC facility at TRIUMF delivers an ionized beam of francium to the FTF where it enters our capture vacuum chamber, strikes and embeds itself onto a neutralizer foil. This foil is attached to a commercial pneumatic rotating apparatus, as modeled in Figure 4.6(a).

The original rotating neutralizer concept was first developed in Stony Brook by collaborators in the early 2000's [27]. First applications of this technique at TRIUMF used an MDC ABRM-133-01 pneumatic rotator. This model has rubber bellows that were only guaranteed by the manufacturer to operate within 80,000 rotation cycles. If we were to run continuously with a ten second cycle, the flapper would only be guaranteed to function for the first ten days, about the same duration and operating conditions of a single beam time. A recent development made by A.I. Gorelov was to replace the MDC flapper unit with a Thermionics unit (FRM-133-25/PNM/ACV-24/CCW/CL) with bellows guaranteed to operate within 800,000 cycles, which has significantly improved the lifetime of this system.

Shown in Figure 4.6(b), our custom foil mount has two arms separated by a cylinder of

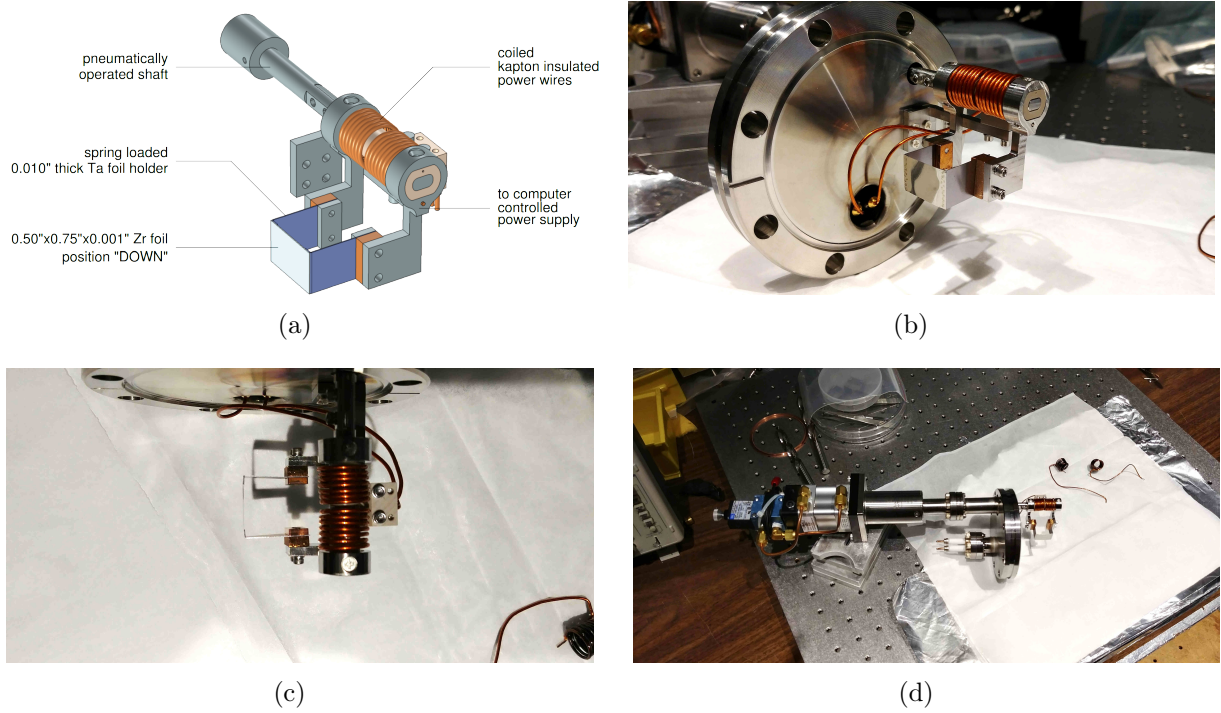


Figure 4.6: Model and photographs of our zirconium foil mounted on our custom flapping apparatus designed and constructed by A.I. Gorelov.

the insulating, ultra high vacuum safe polymer, polyether ether ketone, commonly known as PEEK. Each arm is connected by a Kapton insulated wire coiled around the PEEK cylinder. Coiling this wire greatly reduces the stress and torque applied to the wire during our repetitive flapping motions. The Thermionics shaft and power supply feedthrough leads that connect to the coiled wire can be accessed through two 1.33" ConFlat (CF) reducer flanges installed on a custom 4.5" CF flange.

Early designs of our foil flapper included a 0.001" thick yttrium foil spot-welded onto stainless steel mounting columns. Yttrium was chosen because of its low work function of 3.6 eV compared to the 4.1 eV ionization energy of francium. When the foil is heated, both ionized and neutralized francium will emanate from the surface. Using yttrium, having a

lower work function than the ionization energy of francium, results in less than half of all emitted francium remaining ionized, contributing more neutral atoms to our capture MOT. In practice, however, yttrium proved difficult to work with as it was challenging to spot-weld a material combustible in air at 400 °C [28]. It was also a fragile material that became even more susceptible to being destroyed during the regular heating cycles our francium capture methods require. It was believed that the heating cycles stretched and contracted the material, weakening the welded locations to the solid stainless steel mounting columns. This concept led to the development of 0.010" thick, spring-loaded tantalum mounts for the foil present on our current system, but this did not improve the performance of the foil; the yttrium foil continued to fail at the location of the spot welds, as shown in Figure 4.7.

The decision was eventually made to replace our yttrium foil with one made of zirconium, a significantly more robust material lending itself to simpler spot-welding techniques and being less sensitive to damage from our cyclic heating. Zirconium has a work function of 4.0 eV, almost identical to the ionization energy of francium. This results in a slightly worse trapping efficiency of incoming francium ions, but this has not posed a problem so far. Though zirconium is easier to work with, some care needs to be taken during the heating cycles of the foil. At room temperature, zirconium exists in a hexagonally close-packed crystal structure, but heating above 863 °C causes a phase transition to a body-centered cubic structure [29]. We have observed that heating and cooling foils beyond this temperature while still well below the melting point of zirconium (1855 °C) causes them to resemble ‘Swiss cheese’, as shown in Figure 4.7. In these instances, the foils were effectively ruined and needed to be replaced.

In our experience, yttrium foils needed to be replaced after every beam time whereas the

zirconium foils do not need to be replaced if we operated below $863\text{ }^{\circ}\text{C}$, thus the benefits of using zirconium outweigh its drawbacks, and we will continue to use it in future studies.

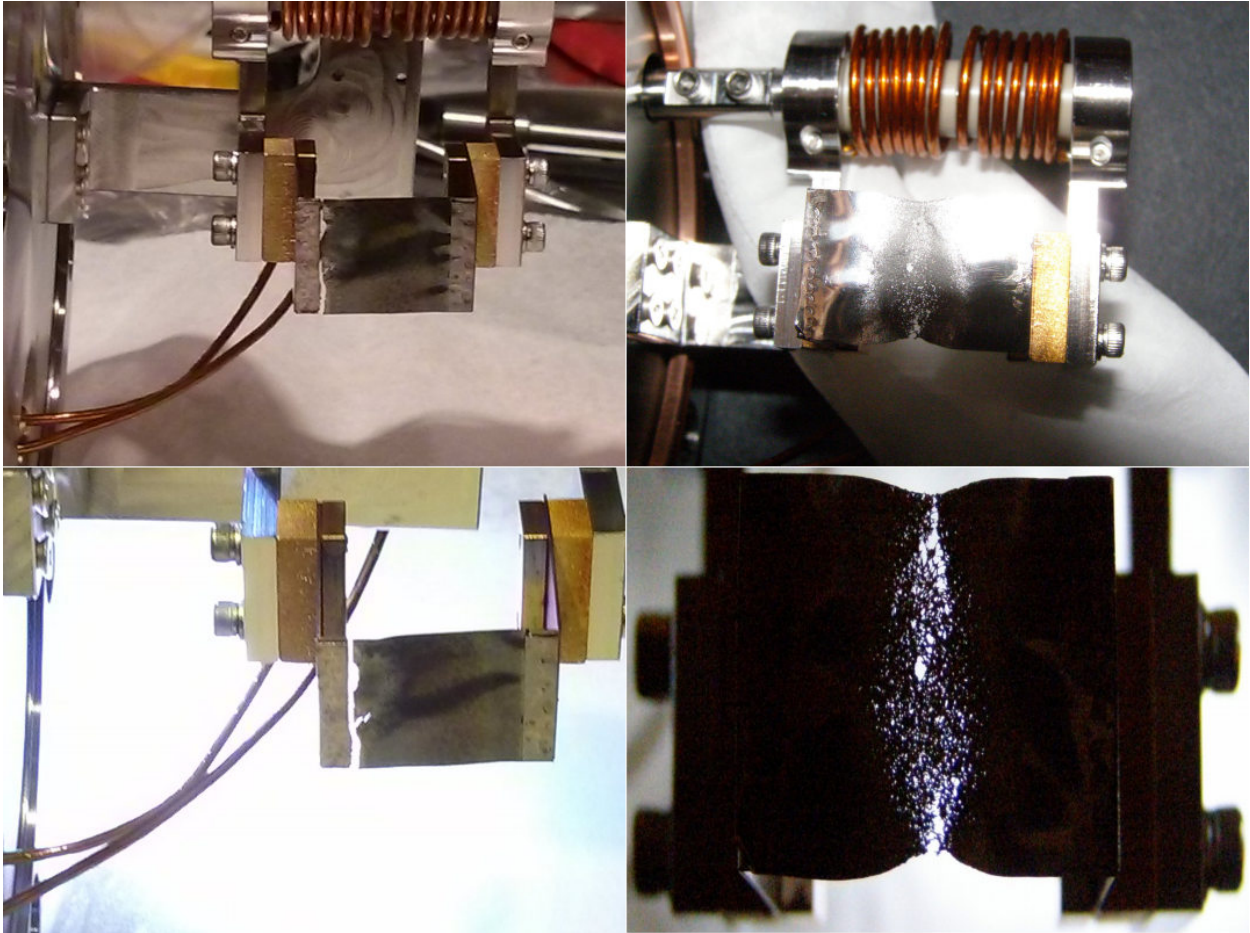


Figure 4.7: Images of damaged yttrium (left) and zirconium (right) foils. The yttrium foil was damaged during standard operating conditions at one of the spot-weld locations. The zirconium foil was damaged when its temperature exceeded the $863\text{ }^{\circ}\text{C}$ phase transition resulting in ‘Swiss cheese’ features. These figures were reproduced with permission from A.I. Gorelov who first presented them at Division of Atomic, Molecular, and Optics Physics (DAMOP) 2016.

Appendix C

Neutralizer Safety Upgrades

During the August 2016 beam time, a glitch in our system allowed current to flow through our neutralizer for an estimated half hour. The neutralizer installed at the time was destroyed and the dryfilm coating on our capture chamber glass cell was believed to be damaged. To prevent this from happening again in the future, we reviewed our neutralizer safety methods and implemented two new analog safety systems.

The power supply that heats the neutralizer (Kepco ATE 25-20M) has a programming block on the back soldered onto a DIN 5-pin cable. It was installed in such a way that the ground and pins 2, 3, and 5 of the cable should always remain grounded where pins 1 and 4 will have 0 V or 5 mV of potential. 5 mV will cause the power supply to run at full current as limited by the front panel setting where 0 V will cause the power supply to output no current.

Following Figure 4.8, a TTL from our controller computer was previously sent to the neutralizer current timer interlock (known as ‘Rob’s box’) which programmed the Kepco to send current to the foil [17]. In the new system, a TTL from the controller goes to

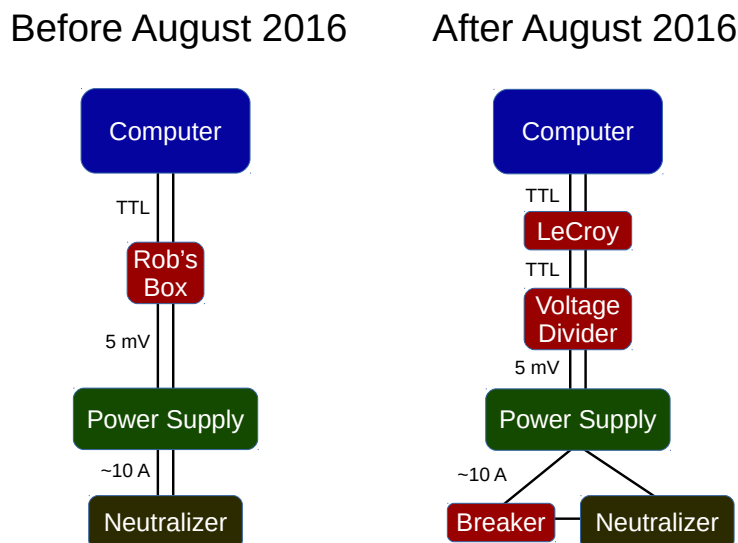


Figure 4.8: These diagrams show the signal paths for how we heat and protect our neutralizer before and after the August 2016 beam time.

a LeCroy Gate Generator (LRS 222). A 3.5 V TTL signal from the LeCroy then passes through a simple homemade voltage divider ($R_1 = 39\text{ k}\Omega$, $R_2 = 56\ \Omega$) to deliver the 5 mV signal required to program the power supply to function as before with Rob's box.

The LeCroy protects the neutralizer by limiting the duration of the output (usually 1 second) and preventing additional input TTLs from initiating another heating cycle before some other set time (usually 15 seconds). Additionally, a simple thermal circuit breaker (SCHURTER TA35 Series 1 Pole) has been put in series with the neutralizer [30]; current on for too long or set too high from the Kepco will trip the breaker, preventing the flow of current to the foil and preventing its destruction. We have several different current rated breakers to allow us to fine tune the duration and amount of current we want to permit to flow through our neutralizer. For any given breaker, there is a non-linear relationship between

current passing through the breaker and the time it takes before it trips, as illustrated in Figure 4.9. For most of our experiments, we have been content with the 4 A rated model where we usually step up or down an Ampere depending on what test we are performing.

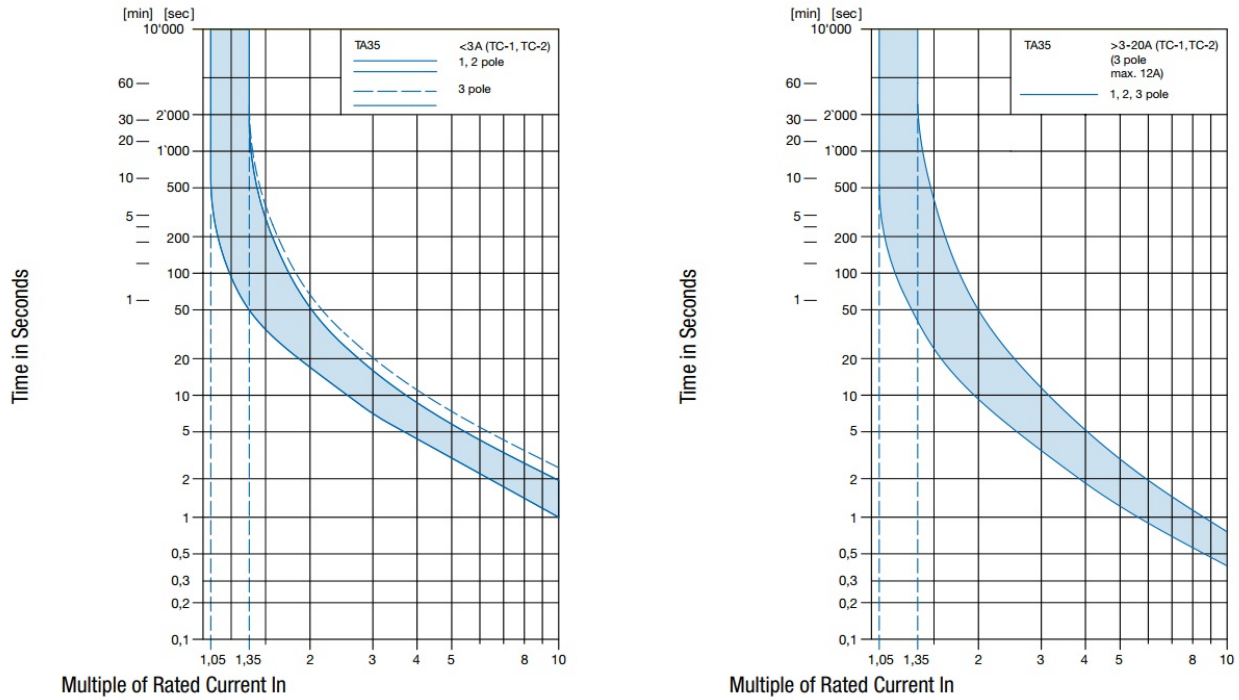


Figure 4.9: This current-time curve is from the user manual for the TA35 Rocker 1Pole series and helps us predict how quickly our breakers will react to overheating our neutralizer [30]. Figures reproduced with permission from Schurter.

Appendix D

OTS Cell Coating

The beam time glitch mentioned in Appendix C gave us the opportunity to experiment with a new cell coating method. Having a ‘dryfilm’ on the cell allows atoms to bounce into the cell and become trapped instead of immediately attaching themselves on the cell surface. Previously, our cell was coated with dichloromethylsilane (SC-77). This procedure included bonding the dryfilm onto the Pyrex surface by exposing the cell to an invisible vapor, depositing an invisible coating with no clear indication as to when the process was sufficiently completed. Only subsequent water drop tests (described later) and francium beam time would confirm the success of the SC-77 dryfilm coating process.

The collaboration decided recently to try a different type of coating that can be deposited in a more controlled way in the liquid phase using octadecyltrichlorosilane, or OTS [5, 31]. Having a more controlled coating procedure also means the performance of the cell can be more consistent between consecutive coatings. In principle, OTS should perform similarly to SC-77, but this still has to be demonstrated experimentally with francium.

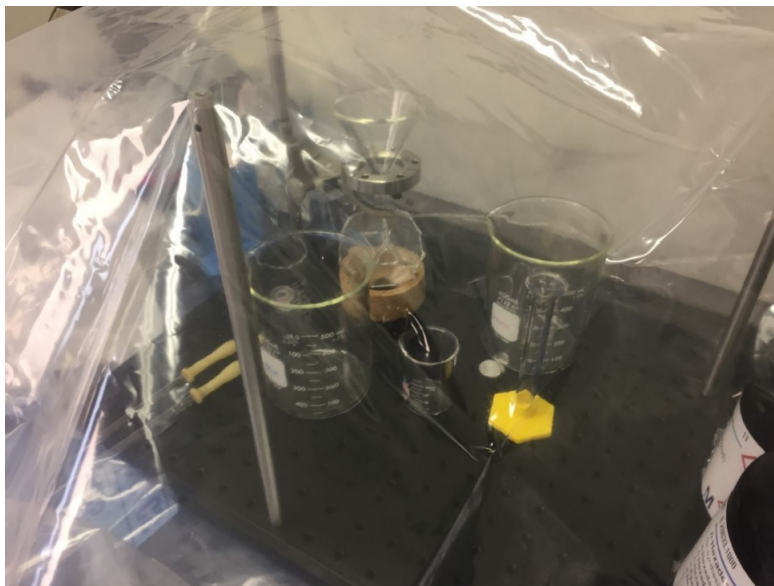


Figure 4.10: This is an image of our cell, glassware, and solvents in a glove bag before applying the OTS solution.

Table 4.1: OTS Coating Procedure [31]

1. Remove previous dryfilm coating with a solution of 10% KOH, 45% water, and 45% ethanol. This step may take several hours where a water drop test can indicate the progress of this step.
2. Pour out the KOH solution and rinse several times with deionized water.
3. Note that octadecyltrichlorosilane (OTS) reacts with water in air, so all solvents and tools need to be prepared in a glove bag pumped with dry nitrogen, argon, or some neutral, dry equivalent for the next two steps.
4. Prepare a solution of 80% n-hexadecane, 8% chloroform, 12% CCl_4 , and 1.9 g OTS per liter of solution.
5. Pour the OTS solution into the cell and wait two minutes. After which, slowly pour out the solution.
6. Bake out cell in vacuum at 200°C for 24 hours.

Throughout the OTS coating process, we performed simple water drop tests to determine the presence of the hydrophobic coating. After stripping the original coating, a drop of water was placed on the cell and reacted as if the surface was hydrophilic, fanning out. After the OTS coating procedure, another water drop test was done on a non-critical component of

the cell where the droplet was observed to bead up as if on a hydrophobic surface as we would expect.

This OTS coating procedure has been performed two times on our cell at the time of writing this thesis. In December 2017, we were given the opportunity to trap ^{86m}Rb and test our atom neutralizing-capturing system. Radioactive rubidium was sent to our capture trap with 700,000 atoms per second resulting in an approximate trap size of 24,000 atoms at a time. In the past we have trapped approximately one million francium atoms where francium was sent to our capture trap at a rate of 10^7 atoms per second. If our rubidium was delivered at the same rate as francium, we would have maintained a trap of about 357,000 atoms. Considering the lifetime of ^{86m}Rb is about a third of the lifetime of our favorite francium isotopes we study and that our lasers are more powerful when tuned to francium-trapping frequencies, the equivalent trap size of ^{86m}Rb would be comparable to francium traps we have produced. In conclusion, we find OTS performs comparably to SC-77 with the benefit of having a simpler and more consistent coating procedure. We will continue to use OTS in future studies.

Appendix E

Software

Programming became a useful tool when estimating the number of atoms we have trapped, monitoring the temperature of the new ULE cavity system, and processing Stark shift data. All software developed and data reduced in this thesis can be found in an online repository (goo.gl/gZtmW5). Below are the names of the programming projects I developed, the files they used, the programming environment they required, and a description of the projects themselves.

Live Binning

(*binsum7.py* in Python 3.5):

While initially taking Stark shift data, we usually have only an approximate frequency of the $ns \rightarrow (n+1)s$ transition for our given sample. We begin with several test scans where we think the resonance should be, but there is a very real possibility that we would misidentify a faint signal as noise. To amplify the presence of real signals while taking data, I wrote a Python script to identify the newest data recorded on our local machines, sum the bins of

a set of scans, bin them again depending on initial user input, and plot the results. This process would repeat within a few seconds, giving operators a live report of binned data to help identify when our scans were resonant with our atoms.

Processing Stark Shift Data

(fn.py, correctmainV.py, & fitstark4.py in Python 2.7):

We use a photomultiplier tube (PMT) to count photons and help us identify when we are resonant with our atoms while doing $ns \rightarrow (n+1)s$ spectroscopy. We scan our lasers in small frequency steps and collect a few milliseconds of PMT counts each step. Our data collecting results in text files with a few hundred lines describing the photon counts and the frequency our probing lasers were set to at that step in the scan. *main.py* is the primary script used to fit a double-Lorentzian curve on the raw data, which is appropriate for the scanning techniques we use. To do so, the script reads a *scans.dat* file in the directory of the raw data which contains the names of sets of scans, and the potential across our field plates at the time of each set. *correctmainV.py* then calls several functions from *fn.py*, a script containing all of the functions used during this data reduction process including binning, taking rolling averages, summing a set of scans, performing fitting procedures with iMinuit, and plotting results. After calling *fn.py* and producing best fit parameters with iMinuit, *correctmainV.py* then produces plots of processed scan sets, as shown in Figure 3.3, one at a time to allow the user to save the results if needed. After every plot, the best fit parameters from iMinuit are also appended to an *out.dat* file to be used by the script *fitstark4.py*. This final script makes a plot of the frequency of the $ns \rightarrow (n+1)s$ transition (and its uncertainties determined by

iMinit in *correctmainV.py*) versus the potential applied across the atoms during the scan. *fitstark4.py* also uses iMinit to fit an exponential curve over these points, where the result of this fit leads us to determine the scalar polarizability of our atoms.

Report ULE Temperature

(*report.sh* & *Linux_Commands.txt* in Bash):

We monitor the temperature of our room and ULE vacuum chamber using thermistors and a Raspberry Pi (R-Pi). Temperatures are continuously sampled once a minute where *report.sh* automatically navigates to the newest file produced by the R-Pi, parses the last line of the file, and prints it in terminal. This can also be used to verify that the R-Pi is actively taking data as this script also reports the time stamp of the last data taken. The file *Linux_Commands.txt* contains a lot of helpful commands to help new users navigate our R-Pi unit, launch the data collecting scripts, and scp data from the machine.

Atom Calculator GUI

(*calc.py*, Python 3.5):

This script runs a graphical user interface (GUI) to help users at our lab calculate the number of atoms we are trapping in our science chamber based on a calculation developed by M. Kalita. We have cameras pointed at our MOT that report the brightness of the trap as well as the background brightness. The cameras also have known exposure times and solid angles relative to the trap which contribute to this calculation. The user enters in values, such as the wavelength of the trapping light, the power of the trapping beams, the beam diameters,

lifetime of the excited state of our atom, the red frequency detuning of the trapping light, as well as region of interest counts and background counts from the cameras. Depending on the uncertainty of the input values, we can then approximate the number of atoms in our trap.

IGBT Switching Plot

(*igbt2.py*, Python 2.7):

While examining the performance of the IGBT switch, I exported data points from an oscilloscope to comma-separated variable (CSV) files. This script is responsible for simply plotting this data as shown in Figure 4.5. The script may be useful to future collaborators in the event they need to employ a vertical break in their plots.

Bibliography

- [1] William J. Marciano and Jonathan L. Rosner. “Atomic parity violation as a probe of new physics”. In: *Phys. Rev. Lett.* 65 (24 Dec. 1990), pp. 2963–2966. DOI: 10.1103/PhysRevLett.65.2963.
- [2] M. A. Bouchiat and C. Bouchiat. “I. Parity violation induced by weak neutral currents in atomic physics”. In: *Journal de Physique* 35.12 (1974), pp. 899–927. DOI: 10.1051/jphys:019740035012089900.
- [3] Ross Diener, Stephen Godfrey, and Ismail Turan. “Constraining extra neutral gauge bosons with atomic parity violation measurements”. In: *Phys. Rev. D* 86 (11 Dec. 2012), p. 115017. DOI: 10.1103/PhysRevD.86.115017.
- [4] R. Carlini for the Qweak collaboration talk at PANIC 2017.
- [5] J. C. Camparo. “Alkali $\langle I \cdot S \rangle$ wall relaxation in dichlorodimethylsilane coated resonance cells”. In: *The Journal of Chemical Physics* 86.3 (1987), pp. 1533–1539. DOI: 10.1063/1.452190.
- [6] E. L. Raab et al. “Trapping of Neutral Sodium Atoms with Radiation Pressure”. In: *Phys. Rev. Lett.* 59 (23 Dec. 1987), pp. 2631–2634. DOI: 10.1103/PhysRevLett.59.2631.

- [7] Claudia Oliveira. “Highly Forbidden Transitions in Alkalis: Preparations for a Parity Violation Experiment”. PhD thesis. 2010. ISBN: 9780494701843.
- [8] W. Z. Zhao et al. “A computer-based digital feedback control of frequency drift of multiple lasers”. In: *Review of Scientific Instruments* 69.11 (1998). DOI: 10.1063/1.1149171.
- [9] M. R. Kalita et al. *Isotope Shifts in the $7s \rightarrow 8s$ Transition of Francium: Measurements and Comparison to *ab initio* Theory*. Oct. 2017. DOI: 10.1103/PhysRevA.97.042507.
- [10] J. Alnis et al. “Subhertz linewidth diode lasers by stabilization to vibrationally and thermally compensated ultralow-expansion glass Fabry-Pérot cavities”. In: *Phys. Rev. A* 77 (5 May 2008), p. 053809. DOI: 10.1103/PhysRevA.77.053809.
- [11] *192-103LEV-A01 Discrete Thermistors*. Honeywell. May 2006. URL: <https://media.digikey.com/pdf/Data%20Sheets/Honeywell%20Sensing%20&%20Control%20PDFs/192-103LEV-A01.pdf>.
- [12] M. R. Kalita. “Search for a Permanent Electric Dipole Moment of ^{225}Ra ”. PhD thesis. University of Kentucky, 2015. URL: http://uknowledge.uky.edu/physastron_etds/34/.
- [13] John S. Steinhart and Stanley R. Hart. “Calibration curves for thermistors”. In: *Deep Sea Research and Oceanographic Abstracts* 15.4 (1968), pp. 497–503. ISSN: 0011-7471. DOI: [https://doi.org/10.1016/0011-7471\(68\)90057-0](https://doi.org/10.1016/0011-7471(68)90057-0).
- [14] E. D. Black. “An introduction to Pound-Drever-Hall laser frequency stabilization”. In: *American Journal of Physics* 69.1 (2001), pp. 79–87. DOI: 10.1119/1.1286663.

- [15] *LiNbO₃ modulators and ModBox for NIR laser applications*. iXblue. 2015. URL: https://photonics.ixblue.com/files/files/pdf/iXBlue_-_Technical_and_Markets_Introduction_of_LiNbO3_modulators_for_NIR_laser_application.pdf.
- [16] Klaus Wendt. *RIMS: Principle and Realization*. URL: <http://www.physik.uni-mainz.de/Larissa/Seiten/Unterseiten/Method.html>.
- [17] R. Collister. “Towards atomic parity violation at the francium trapping facility”. PhD thesis. University of Manitoba, 2015. URL: <http://hdl.handle.net/1993/31082>.
- [18] Philip D Harvey. *Engineering properties of steel*. Asm Intl, 1982. ISBN: 9780871701442; 0871701448.
- [19] John E. Simsarian. “Laser spectroscopy and lifetime measurements on trapped francium”. PhD thesis. 1998. ISBN: 9780599116801; 0599116803. URL: <https://search-proquest-com.ezproxy.library.ubc.ca/docview/304485532?accountid=14656>.
- [20] W. H. King. “Comments on the Article “Peculiarities of the Isotope Shift in the Samarium Spectrum””. In: *J. Opt. Soc. Am.* 53.5 (May 1963), pp. 638–639. DOI: 10.1364/JOSA.53.000638.
- [21] C. S. Wood et al. “Measurement of Parity Nonconservation and an Anapole Moment in Cesium”. In: *Science* 275.5307 (1997), pp. 1759–1763. ISSN: 00368075, 10959203. DOI: 10.1126/science.275.5307.1759.
- [22] M. S. Safronova, W. R. Johnson, and A. Derevianko. “Relativistic many-body calculations of energy levels, hyperfine constants, electric-dipole matrix elements and static polarizabilities for alkali-metal atoms”. In: (1999). DOI: 10.1103/PhysRevA.60.4476.

- [23] S. Bennett, J. Roberts, and C. Wieman. “Measurement of the dc Stark shift of the $6S \rightarrow 7S$ transition in atomic cesium”. In: *Physical Review A* 59.1 (1999), R16–R18. DOI: 10.1103/PhysRevA.59.R16.
- [24] J Mitroy, M S Safronova, and Charles W Clark. “Theory and applications of atomic and ionic polarizabilities”. In: *Journal of Physics B: Atomic, Molecular and Optical Physics* 43.20 (2010), p. 202001. DOI: 10.1088/0953-4075/43/20/202001.
- [25] Stanford Research Systems. *High Voltage Power Supplies: PS355, PS365, PS370, PS375*. Version 1.0. URL: <http://thinksrs.com/downloads/PDFs/Manuals/PS365m.pdf>.
- [26] *STGE50NC60WD*. STMicroelectronics. 2007. URL: <http://www.st.com/content/ccc/resource/technical/document/datasheet/group2/79/ba/9a/5d/58/57/46/98/CD00159057/files/CD00159057.pdf/jcr:content/translations/en.CD00159057.pdf>.
- [27] S. Aubin et al. “High efficiency magneto-optical trap for unstable isotopes”. In: *Review of Scientific Instruments* 74.10 (2003), pp. 4342–4351. DOI: 10.1063/1.1606093.
- [28] D. R. Lide. *CRC handbook of chemistry and physics: a ready-reference book of chemical and physical data*. CRC Press, 2008. ISBN: 9781420066791.
- [29] I. Schnell and R. C. Albers. “Zirconium under pressure: phase transitions and thermodynamics”. In: *Journal of Physics: Condensed Matter* 18.5 (2006), p. 1483. DOI: <https://doi.org/10.1088/0953-8984/18/5/001>.
- [30] *TA35 Rocker 1Pole*. SCHURTER. Mar. 2017. URL: https://us.schurter.com/bundles/sneceschurter/epim/_ProdPool_/newDS/en/typ_TA35_Rocker_1Pole.pdf.

- [31] J.A. Fedchak et al. “Silane coatings for laser-driven polarized hydrogen sources and targets”. In: *Nuclear Instruments and Methods in Physics Research Section A: Accelerators, Spectrometers, Detectors and Associated Equipment* 391.3 (1997). ISSN: 0168-9002. DOI: [https://doi.org/10.1016/S0168-9002\(97\)00571-8](https://doi.org/10.1016/S0168-9002(97)00571-8).